Biophysical *Journal*
Article

Biophysical Society

Intestinal villus structure contributes to even shedding of epithelial cells

Yuto Kai[1,*]
[1]Department of Anatomy and Cell Biology, Graduate School of Medical Sciences, Kyushu University, Fukuoka, Japan

ABSTRACT In the intestinal epithelium, proliferated epithelial cells ascend the crypts and villi and shed at the villus tips into the gut lumen. In this study, we theoretically investigate the roles of the villi on cell turnover. We present a stochastic model that focuses on the duration over which cells migrate the shortest paths between the crypt orifices and the villus tips, where shedding cells are randomly chosen from among those older than the shortest-path cell migration times. By extending the length of the shortest path to delay cell shedding, the finger-like shape of the villus would tightly regulate shedding-cell ages compared with flat surfaces and shorter projections; the villus allows epithelial cells to shed at around the same age, which limits them from shedding early or staying in the epithelium for long periods. Computational simulations of cell dynamics agreed well with the predictions. We also examine various mechanical conditions of cells and confirm that coordinated collective cell migration supports the predictions. These results suggest the important roles of the villi in homeostatic maintenance of the small intestine, and we discuss the applicability of our approach to other tissues with collective cell movement.

SIGNIFICANCE The intestinal villi are numerous finger-like structures covered by epithelial cells and projecting into the gut lumen. The villi are well known for expanding the gut surface area for efficient absorption; we suggest that they also contribute to tight regulation of cell turnover. The villi limit epithelial cells from shedding early or remaining in the epithelium for long periods by separating the villus tips, where cells shed, from the crypts, where cells are produced. Here, we propose even shedding of epithelial cells as another role of the villi and underline their physiological and pathophysiological importance.

INTRODUCTION

The small intestine owes most of its nutrient-absorptive surface area to the villi—numerous finger-like structures protruding into the lumen from the intestine's wall covered by a single layer of cells, most of which are absorptive epithelial cells (1). The villi are 400–1000 μm tall in humans (2) and 150–400 μm tall in mice (3) and contribute an absorptive surface area ~6.5 times greater than a simple cylindrical intestine of the same diameter and length would (4). Hence, the villous atrophy observed in conditions such as celiac disease or Crohn's disease often severely hampers absorption (5,6).

The small intestine has the fastest cell turnover in the body. Its epithelial cells are renewed every 3–5 days by repeating cycles of cell proliferation, migration, and shedding (7–9). Each villus is surrounded by several invaginations called crypts. Intestinal stem cells at the crypt base divide with cell cycles of ~12–24 h (10,11). Daughter cells differentiate within the crypts, then ascend the crypts, and then migrate to the nearest villus. Upon reaching the villus tip, the cells shed into the gut lumen. The small intestine is considered to maintain its homeostasis by replacing epithelial cells and filling its surface with fresh cells while keeping the total epithelial cell number constant (12). This continual renewal process enhances the assimilation and protection of the small intestine (13).

To elucidate cell turnover mechanisms in the small intestine, previous studies have explored cell proliferation and cell behavior in the intestinal crypts (14–18), driving forces of cell movement in the villus epithelium (19–22) and cell-shedding processes at the villus tips (23,24). Furthermore, the influences of pathological factors, such as inflammation or infection, on cell motility in the epithelium or cell turnover of the small intestine have been investigated (25,26). On the other hand, to our knowledge, few studies have focused on the effects of the villus shape itself on normal cell turnover of the small intestine.

Submitted June 18, 2020, and accepted for publication January 8, 2021.
*Correspondence: yuto0730@med.kyushu-u.ac.jp
Editor: Mark Alber.
https://doi.org/10.1016/j.bpj.2021.01.003
© 2021 Biophysical Society.

In this study, we theoretically investigate the roles of the villus on cell turnover and propose that its finger-like shape tightly regulates shedding-cell ages; the villus limits epithelial cells from shedding early or staying in the epithelium for prolonged periods. In the Methods, we provide some details of the three-dimensional (3D) surface and the two-dimensional (2D) plane cell-based dynamic models. In the Results, focusing on the time when cells migrate over the shortest paths between the crypt orifices and the cell-shedding sites, we begin by presenting a stochastic model that describes cell turnover of tissues with collective cell migration and examine the effects of the height or shape of the villus on the spread of shedding-cell ages. Using this model, we then numerically predict the distributions of shedding-cell ages for three structures with different shapes. Next, we computationally simulate the 3D surface cell-based model for three geometries and compare the results with the predictions of the stochastic model. Lastly, we build the simplified 2D plane cell-based model for two flat regions with different lengths and address the effects of active cell migration and different material properties of cells on shedding-cell age distributions. We also discuss the applicability of our approach to other tissues with collective cell movement.

METHODS

3D surface cell-based model

We performed computational simulations of a 3D surface cell-based model using an off-lattice overlapping sphere model developed by Mirams et al. (27). We constructed three geometries: Villus, Bump, and Disk, as shown in Fig. 3 *A* and Fig. S2. Times, in the model, are measured in cell hours, and units of space are cell diameters (CDs). The Villus has a finger-like shape, the Bump has a hemisphere-like shape, and the Disk has a flat circular surface. Sizes are scaled so that each structure has approximately the same cell number: 600 cells was chosen for a practicable simulation cost. Each structure is surrounded by eight crypts following the murine intestine (28). Each structure also has one shedding site at its tip or center. Cells proliferated in the crypts move over the surfaces and shed at the shedding sites. Because of the scaling for approximately the same cell number, the length of the shortest path from the crypt orifices to the shedding site is longest in the Villus, followed by the Bump and finally the Disk (Fig. S2).

Cells are modeled as a set of nodes, each of which represents a cell center. The cells are free to move within the surfaces (29). Cells move according to interactions with neighboring cells, which are determined by whether two cell centers are within a certain interaction distance of 1.5 CDs (27); because the cells move, cell neighborhoods are updated in every time step. Elastic-cell-cell interaction drives local repulsive and attractive forces, and each cell experiences the Hookean linear spring forces that act along the vectors connecting neighboring cell centers (29). For simplicity, all springs are set with the same spring constant. The total force acting on cell i at time t is, therefore, the sum of all elastic forces coming from the springs of all neighboring cells $j \in \mathcal{M}_i(t)$ connecting to cell i at that time, given by the following:

$$\mathbf{F}_i(t) = \mu \sum_{j \in \mathcal{M}_i(t)} \widehat{\mathbf{r}}_{i,j}(t)\big(\|\mathbf{r}_{i,j}(t)\| - s_{i,j}(t)\big), \tag{1}$$

where μ is the spring constant, $\mathbf{r}_{i,j}(t) = \mathbf{r}_j(t) - \mathbf{r}_i(t)$ is the vector from the center of cell i to the center of cell j at time t, $\widehat{\mathbf{r}}_{i,j}(t)$ is the corresponding unit vector, and $s_{i,j}(t)$ is the natural length of the spring connecting cells i and j at time t. The natural length is 1.0 CD for all cells unless cells i and j are a pair of dividing cells. When a cell divides, $s_{i,j}(t)$ increases linearly from 0.3 CD to 1.0 CD over the first cell hour to represent cell growth (30). By making the simplifying assumption that internal terms are sufficiently small compared with dissipative terms (31), cell inertia is neglected, and we obtain the following first-order equation of motion for cell i:

$$\eta \frac{\mathrm{d}\mathbf{r}_i}{\mathrm{d}t} = \mathbf{F}_i(t), \tag{2}$$

where $\mathbf{r}_i$ is the vector of the cell center i, and η is the drag coefficient representing the cell-substrate adhesion. We solve this equation numerically using the forward Euler method with a time step Δt sufficiently small to achieve numerical stability. Thus, the effective displacement of each cell center i within Δt is given by

$$\mathbf{r}_i(t + \Delta t) = \mathbf{r}_i(t) + \frac{1}{\eta}\mathbf{F}_i(t)\,\Delta t. \tag{3}$$

Proliferative and differentiated cells are determined by their locations. Cells located in the crypts behave as proliferative cells and so can divide. Cells outside the crypts are differentiated cells that cannot divide. Each cell has an individual cell age that increments every time step. Each proliferative cell is assigned to a randomly chosen cell division interval, after which it will supply a cell naturally into the surface. When a cell divides, a daughter cell is placed within the crypt surface with its center 0.3 CD away from the center of the mother cell in a randomly chosen direction (30). Their cell age is then reset to 0, and new division intervals are assigned. Cells moved outside the surface are returned to it perpendicularly in the next time step. Cells emerging from the crypts change into differentiated cells, which move across the surfaces and ultimately shed at the shedding sites.

When cell centers move above the threshold heights of the Villus or Bump or approach within a threshold distance of the Disk center, they are removed (27,32). Associated springs are removed at this time, and spring connections are not formed within the shedding sites. The shedding sites' heights or diameters are chosen to give similar cell-shedding rates and shedding behavior among structures when equal cell proliferation rates are given. Cells are not removed other than at the shedding sites. Cell movement is, therefore, passively driven by mitotic pressure of the proliferative cells and by the negative pressure of cell shedding (29). The determination of other parameter values and dimensions is described in Supporting materials and methods, Appendix S7 *a*.

2D plane cell-based model

The 2D plane cell-based model is also an off-lattice overlapping sphere model. We built two flat rectangular geometries with different lengths: Long and Short, as shown in Fig. 4 *A*. Times are measured in cell hours and distances are measured in CDs. Both shapes have one crypt and one shedding site, and their dimensions are set to have ~200 cells in total (Figs. S4, *A* and *B*). The mechanics of cell movement are the same as in the 3D model. We represent cell centers by nodes that are free to move within the surfaces. Cells are deemed neighbors if their centers are within the interaction distance of 1.5 CDs, and to allow for changes due to cell movement, cell neighborhoods are updated at every time step. The force on each cell is the sum of the forces due to interactions with neighboring cells, calculated as a Hookean linear spring force (Eq. 1). Again, the equation of motion and displacement of each cell center is expressed by Eqs. 2 and 3, μ is the spring constant connecting cells, η is the drag coefficient acting on cells, and the natural length of connecting springs is 1.0 CD except for cell division.

Cells located in the crypts are proliferative, and the others are differentiated. Each cell has an age that increments from its birth. A proliferative cell

divides when its cell age exceeds a randomly assigned division interval. At that moment when a cell divides, a daughter cell is placed 0.3 CD away from the center of the mother cell in a randomly chosen direction within the crypt surface, and the natural length of the spring increases linearly from 0.3 CD to 1.0 CD over the first cell hour. Then, their cell age is reset to be 0, and new division intervals are assigned. Cells pushed out of the surface return perpendicularly into the surface in the next time step. Differentiated cells move over the surfaces and shed at the shedding sites. Cells are removed when their centers exceed the threshold distances from the crypt orifices; neighboring cells lose the springs connecting with the removed cells. Both shapes have shedding sites of the same width to ensure similar cell-shedding behavior. Cells are not removed other than the shedding sites. Cell movement is, therefore, passively driven by mitotic pressure and negative pressure by cell shedding when an active migration force is not implemented.

In the 2D model, we also examined a case in which cells actively migrate. We introduced an additional active migration force acting on each cell (33), modifying Eq. 2 to

$$\eta \frac{\mathrm{d}\mathbf{r}_i}{\mathrm{d}t} = \mathbf{F}_i(t) + \alpha \widehat{\mathbf{e}_{\mathrm{y}}}, \tag{4}$$

where α is a constant representing the magnitude of the active migration force and $\widehat{\mathbf{e}_{\mathrm{y}}}$ is the unit vector in the direction from the crypt to the shedding site. We solve Eq. 4 numerically. Other parameter values and dimensions were determined as described in Supporting materials and methods, Appendix S7 *b*.

RESULTS

Description of cell turnover by the stochastic model

In this section, we first present a stochastic model of cell turnover that focuses on the time when cells migrate over the shortest paths between the crypt orifices and the shedding sites. Next, we examine the effects of the height or shape of the villus on the spread of shedding-cell ages. We then compare the spread of shedding-cell ages among three structures with different shapes. Lastly, we conduct numerical calculations of the stochastic model for the three structures.

Fig. 1 *A*, left panel, shows the epithelium of the small intestine where a finger-like villus is surrounded by several crypts. Epithelial cells emerge from the crypts, enter and ascend the villus surface, and shed at the villus tip into the gut lumen. Here, we suppose that cells from the crypts directly enter the adjacent villus surface and that cells move collectively in the epithelium to the villus tip. Upon reaching the villus tip, cells are shed by anoikis, where neighboring cells expel those accumulated at the villus tip (23,34). The probability of cell shedding would, therefore, be constant regardless of cell ages or cell types. Furthermore, we do not consider the apoptosis that is occasionally observed outside the villus tip. Cells must hence migrate to the shortest path between the crypt orifices and the villus tip (L_{f}), as indicated by the double line, at least before shedding, and the shedding-cell age would at least exceed the time needed for cells to migrate over the shortest path (τ_{f}).

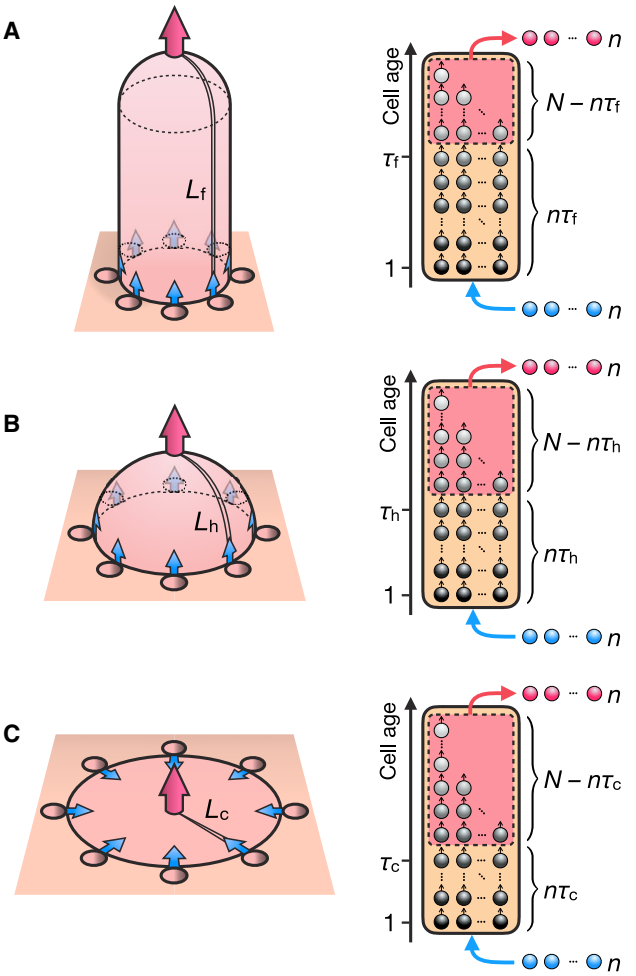

FIGURE 1 Stochastic model of cell turnover. Left panels: given is the schematic description of the finger-like (*A*), hemispheric (*B*), and circular disk (*C*) structures of the epithelium. Cells enter the epithelium from the crypts (*blue arrows*) and shed from the tips or the center of the structures (*red arrows*). L_{f}, L_{h}, and L_{c}, as indicated by double lines, are the lengths of the shortest path between the crypt orifices and the shedding sites. Right panels: shown are the stochastic processes of cell turnover in respective structures. τ_{f}, τ_{h}, and τ_{c} are the cell migration times for the shortest paths of the respective structures. Each structure has a total of N cells in the epithelium and chooses n red-colored cells as the shedding cells from those aged above the shortest-path cell migration times, i.e., the cells surrounded by the dashed-line frames. After the remaining intraepithelial cells have incremented their ages by 1, n blue-colored cells of age 1 are supplied into the epithelium from the crypts. To see this figure in color, go online.

Fig. 1 *A*, right panel, illustrates the stochastic process of cell turnover of the finger-like villus at steady state. There are N cells, in total, in the epithelium. At each time step, n cells are randomly chosen to be the shedding cells from those aged over τ_{f}, intraepithelial-cell ages are incremented by 1, and n cells of age 1 are supplied from the crypts. N remains constant under these conditions. Therefore, the number of cells that cannot shed is $n\tau_{\mathrm{f}}$, the number of cells that

can shed is $N - n\tau_f$, and the probabilities that cells of age t can shed are as follows:

$$\begin{cases} 0, & (t \le \tau_f), \\ \dfrac{n}{N - n\tau_f} = p_f, & (t > \tau_f). \end{cases} \tag{5}$$

Thus, the probability of cell shedding at age t is given by

$$\begin{cases} 0, & (t \le \tau_f), \\ p_f(1 - p_f)^{t-\tau_f-1}, & (t > \tau_f), \end{cases} \tag{6}$$

which has a geometric distribution when $t > \tau_f$. Hence, the expected value of the shedding-cell age is $T = N/n$, and the standard deviation (SD) of the shedding-cell ages is given by (see Supporting materials and methods, Appendix S1)

$$\sigma_f = \sqrt{(T - \tau_f)(T - \tau_f - 1)}. \tag{7}$$

This expression shows that σ_f decreases as τ_f approaches T: the spread of shedding-cell ages decreases as the shortest-path cell migration time approaches the expected value of the shedding-cell age.

We then modeled the finger-like villus as a structure with a hemisphere atop a cylinder (Fig. S1 *A*) and examined how the villus height affects the spread of shedding-cell ages. We define the epithelial surface area as the total surface area surrounded by the crypts. When the height of the finger-like structure is varied while keeping a constant epithelial surface area, L_f lengthens, thereby τ_f increases as the overall villus height increases (see Supporting materials and methods, Appendix S2). Assuming that N and n are constant regardless of the villus height, making T the same, σ_f decreases as the villus height increases (Eq. 7). A taller finger-like villus hence reduces the spread of shedding-cell ages. Next, we discussed the effects of the villus shapes on the spread of shedding-cell ages, e.g., the villus with pointed tip has also been observed in vivo (3). Modeling the pointed villus as a cone for simplicity (Fig. S1 *B*), the conical structure has a longer length of the shortest path between the base and the tip of the structure than that of the finger-like structure for the same epithelial surface area (see Supporting materials and the methods, Appendix S3). The conical structure hence has a smaller spread of shedding-cell ages than the finger-like structure for the same values of N and n. The villi with more pointed tips can also decrease the spread of shedding-cell ages.

To further explore the roles of the finger-like shape of the villus on cell turnover, we then compare three structures—the finger-like, hemispheric, and circular disk structures as shown in Figs. 1 and S1, *A*, *C*, and *D*. All of the structures are surrounded by crypts, and cells shed at the tips or the center of the structures. When all structures have equal epithelial surface areas, the length of the shortest path always decreases in the order of the finger-like, hemispheric, and circular disk structures—$L_f > L_h > L_c$—independently of their scales (see Supporting materials and methods, Appendix S4). Thus, the shortest-path cell migration time also decreases in the same order: $\tau_f > \tau_h > \tau_c$. Assuming that N and n are the same regardless of the structures, making T equal, the finger-like structure has the smallest spread of shedding-cell ages, followed by the hemispheric and circular disk structures, in that order (Eq. 7): $\sigma_f < \sigma_h < \sigma_c$. Here, σ_h and σ_c are the SDs of the shedding-cell ages of the hemispheric and circular disk structures, respectively. The finger-like structure shows more uniform shedding-cell ages than do the hemispheric and circular disk structures.

Finally, we performed numerical calculations on the stochastic model for the three structures: the finger-like, hemispheric, and circular disk structures. As shown in Table 1, we estimated parameter values using experimental results of the murine small intestine (see Supporting materials and methods, Appendix S5; (9,22)). All structures are set to have the same values of N and n but different shortest-path cell migration times. Fig. 2 *A* shows the shedding-cell age distributions. All structures have equal mean shedding-cell ages but differing SDs. For all three structures, the shedding-cell age is distributed geometrically, with the minimal shedding age being associated with the length of the shortest path from crypt to shedding zone. The minimal shedding age is greatest for the finger-like structure, followed by the hemispheric structure, then the circular disk structure. On the other hand, the finger-like structure has the youngest late shedding-cell age, indicated by the 90th percentile of each shedding-cell age distribution, followed by the hemispheric and circular disk structures, in that order. It is expected that the finger-like structure sheds nearly almost all of its cells within 100 h, which agrees with the observations of labeled cells in the murine intestine shedding within 5 days (7). Fig. 2 *B* shows the intraepithelial-cell age distributions. In all structures, the cell frequency is constant until the shortest-path cell migration time and then decreases. The finger-like structure has the lowest average intraepithelial-cell age, followed by the hemispheric structure and then the circular disk structure.

TABLE 1 Estimated parameter values of numerical calculations in the stochastic model

Symbol	Value	Description
N	1885	total number of cells in the epithelium
n	26 h^{-1}	cell supply and shedding rates
τ_f	65 h	the shortest-path cell migration time of the finger-like structure
τ_h	38 h	the shortest-path cell migration time of the hemispheric structure
τ_c	34 h	the shortest-path cell migration time of the circular disk structure

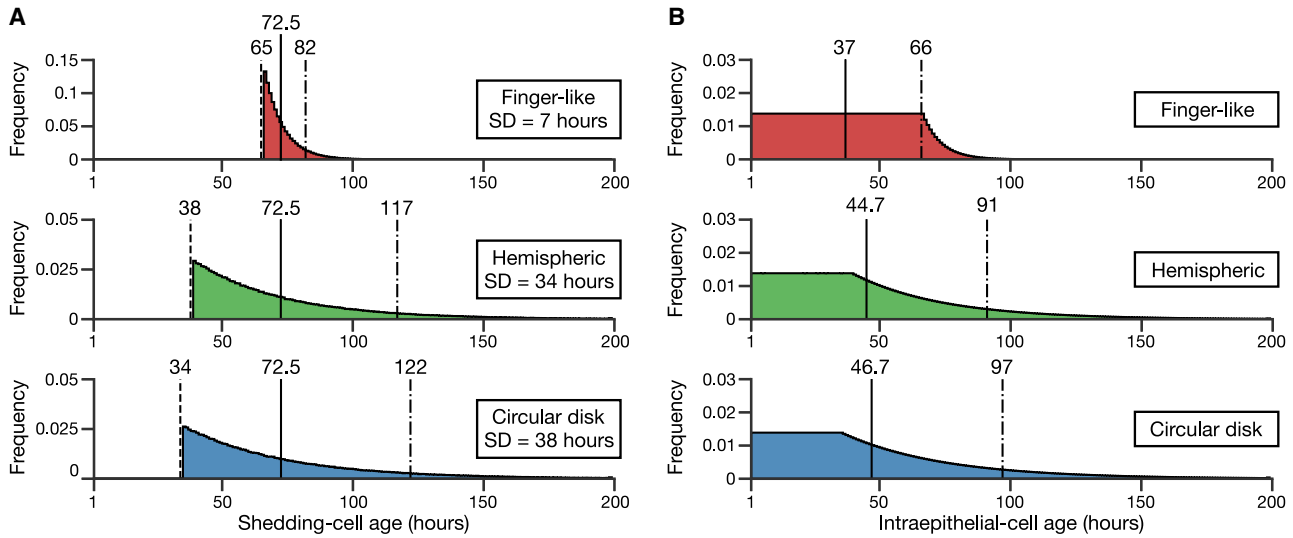

FIGURE 2 Numerical calculations of the stochastic model. (*A*) Shown are the shedding-cell age distributions of the finger-like (*top*), hemispheric (*middle*), and circular disk (*bottom*) structures. Dashed lines, the shortest-path cell migration times; solid lines, the average shedding-cell ages; dot-dash lines, the late shedding-cell ages. (*B*) Shown are the intraepithelial-cell age distributions of the finger-like (*top*), hemispheric (*middle*), and circular disk (*bottom*) structures. The solid lines represent the average intraepithelial-cell ages, and the dot-dash lines represent the old intraepithelial-cell ages. To see this figure in color, go online.

Furthermore, the old intraepithelial-cell age, which is defined as the 90th percentile of each intraepithelial-cell age distribution, increases in the same order. We also confirmed that the SDs of shedding-cell ages and the average intraepithelial-cell ages obtained from the numerical calculation coincide with those calculated analytically (see Supporting materials and methods, Appendix S6). It is hence predicted that compared with the hemispheric or circular disk structures, the finger-like structure reduces the spread of the shedding-cell ages and limits cells from shedding early or staying in the epithelium for long periods.

Investigation by the 3D surface cell-based model

To consider the effects of cell-cell interactions and the geometry of surfaces, we conducted computational simulations of the 3D surface cell-based model and examined whether the results agree with the predictions from the stochastic model. As shown in Fig. 3 *A*, we then constructed three geometries: Villus, Bump, and Disk. Their dimensions are chosen for approximately equal total cell numbers. All structures are also set to have the same numbers and sizes of crypts, which gives the same cell proliferation rates. Cells proliferated in the crypts move on the surfaces and shed at the tips or center of the structures. The length of the shortest path between the crypt orifices and the shedding sites is the longest in the Villus, followed by the Bump and Disk, in that order (Fig. S2).

The cell proliferation rates are set to be equal for all structures, and the equilibrium total cell numbers are uniform over time (Fig. S3 *A*); thus, all structures have approximately the same average cell-shedding rates (Fig. 3 *B*). The average total cell numbers are also approximately equal among structures (Fig. 3 *C*). The Villus and Disk show about the same average cell density, and the Bump has a lower density (Fig. S3 *B*), suggesting that not only the difference in the path length between the crypts and the shedding sites but also the geometrical feature, flat or curved, determines cell density. In addition, slight decreases in cell density from the crypts to shedding sites are shown (Fig. S3 *C*), which echoes the cell-density profiles in the lower villus region (22,35). Fig. 3 *D* shows the shedding-cell age distributions. In all geometries, the peak points of the distributions shift to the right of the respective minimal shedding-cell ages, and left tails appear. The shifts would be due to random cell motion caused by cell-cell interactions, which prevents cells from straight moving from the crypt orifices to the shedding sites (Video S1), and cells that migrate in the shortest times decrease. The average shedding-cell ages are approximately equal among structures, as indicated by the solid lines. On the other hand, the Villus has the smallest SD of the shedding-cell ages, followed by the Bump and then Disk. Dash and dot-dash lines in Fig. 3 *D* indicate the early and late shedding-cell ages that are defined as the 10th and 90th percentiles of the shedding-cell ages, respectively. The Villus has the oldest early shedding-cell ages, followed by the Bump and Disk, in that order. By contrast, the Villus has the youngest late shedding-cell ages, followed by the Bump and Disk, in that order. Fig. 3 *E* shows intraepithelial-cell age distributions. The average intraepithelial-cell age increases in the order of the Villus, Bump, and Disk. The old intraepithelial-cell age, indicated by the 90th percentile of each intraepithelial-cell age distribution, also increases in the same order. The results of the 3D model show the following

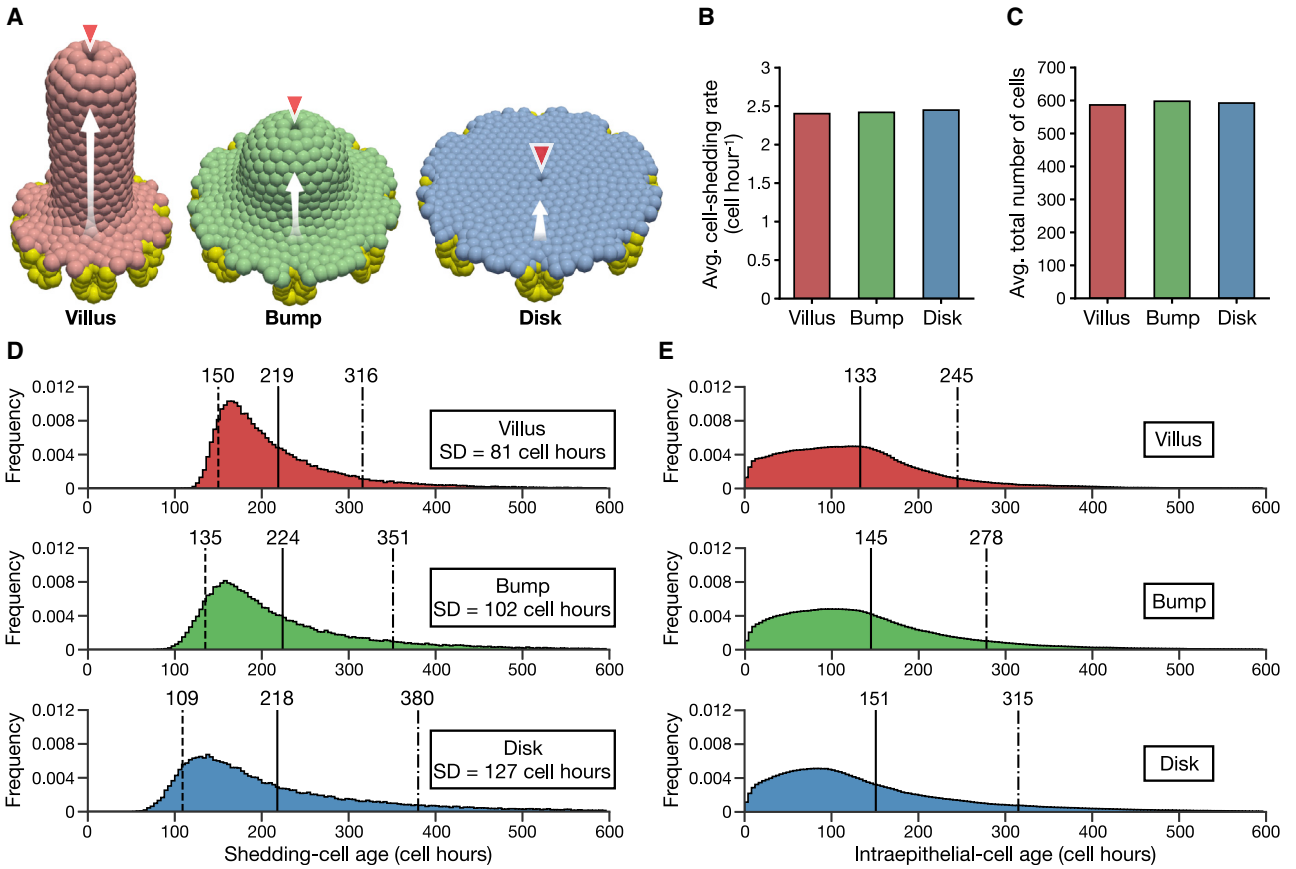

FIGURE 3 Simulations of the 3D surface cell-based model. (*A*) Given are snapshots of the Villus (*left*), Bump (*middle*), and Disk (*right*). Proliferative cells are colored yellow; the other colors indicate differentiated cells. Cells from the crypts move on the surfaces as indicated by the white arrows and are shed at the shedding sites marked by the red arrowheads. (*B*) Given is the average number of cells that shed per one cell hour. (*C*) Given is the average total number of cells in the structures. (*D*) Given are the shedding-cell age distributions of the Villus (*top*), Bump (*middle*), and Disk (*bottom*). Dashed lines, the early shedding-cell ages; solid lines, the average shedding-cell ages; dot-dash lines, the late shedding-cell ages. (*E*) Shown are the intraepithelial-cell or differentiated-cell age distributions of the Villus (*top*), Bump (*middle*), and Disk (*bottom*). The decreased frequency around age 0 is because proliferative cells account for the majority of the population. The solid lines represent the average intraepithelial-cell ages, and the dot-dash lines represent the old intraepithelial-cell ages. To see this figure in color, go online.

compared with the Bump and Disk under equal cell proliferation rates and equal total cell numbers: the Villus reduces the spread of the shedding-cell ages and limits cells from shedding early or staying in the epithelium for prolonged periods. These results agreed well with the predictions of the stochastic model.

Validation of the 2D plane cell-based model

To promote generalization and examine various mechanical conditions of cells, we then built a simplified 2D plane cell-based model using the same framework as the 3D model. As shown in Figs. 4 *A* and S4 *A*, we considered two flat, rectangular geometries with one crypt and one shedding site at opposite ends. They differ in length: Long and Short. Cells increased in the crypts move toward the shedding sites.

We began by examining whether the 2D model shows similar results to the 3D model. Their dimensions and parameter values are determined for the same total cell numbers and same cell proliferation rates; ordered collective cell migration occurs in the upper parts of both shapes (Video S2). The equilibrium total cell numbers are constant over time (Fig. S4 *C*), and both shapes have approximately equal average cell-shedding rates (Fig. 4 *B*). The average total cell numbers are also approximately equal between the two shapes (Fig. 4 *C*). The Long has a higher average cell density than the Short (Fig. S4 *D*), and both show gradual decreases in cell density from the crypts to the shedding sites (Fig. S4 *E*). The shedding-cell age distributions, shown in Fig. 4 *D*, have the same average, but the Long has a narrower range than the Short. Considering the subsequent comparisons with distributions having largely different average shedding-cell ages, the spread of shedding-cell ages is compared using the coefficient of variations (CVs) in the 2D model. The Long has an older early shedding-cell age and younger late shedding-cell age than the Short. Moreover, the Long has a narrower intraepithelial-cell age distribution than the Short (Fig. S4 *F*). These results are

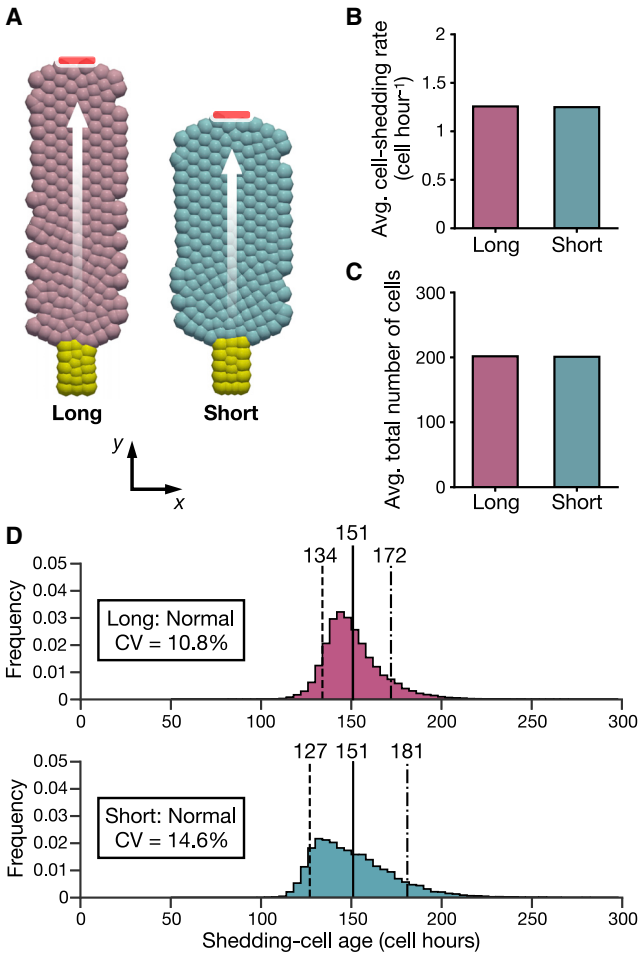

FIGURE 4 Validation of the 2D plane cell-based model: normal results. (*A*) Given are snapshots of the Long (*left*) and Short (*right*). Proliferative cells are colored yellow; other colors are differentiated cells. Cells from the crypts move on the surfaces as indicated by the white arrows and shed at the shedding sites indicated by red markers. (*B*) Given is the average number of cells that shed per one cell hour. (*C*) Given is the average total number of cells in the models. (*D*) Shown are the shedding-cell age distributions of the Long (*top*) and Short (*bottom*). The dashed lines represent the early shedding-cell ages, the solid lines represent the average shedding-cell ages, and the dot-dash lines represent the late shedding-cell ages. To see this figure in color, go online.

similar to those of the 3D model, indicating that the stochastic model predictions are held for the 2D model. We hereinafter refer to the conditions or results of this section as normal.

Effects of active cell migration

Although the renewal of the intestinal epithelium is considered to be driven by the mitotic pressure in the crypts (1,21), active cell migration of an actomyosin-dependent manner has also been proposed to occur in the upper part of the villus (19,22). We then simulated this effect in the 2D model by applying an active migration force in the y axis direction, as expressed by Eq. 4. Here, α is a constant representing the magnitude of the active migration force and varied between 0 and 0.2. The "normal" settings above are used for the other parameter values except for the crypt depth.

We regulate the crypt depth to achieve approximately equal proliferation rates for all conditions, and the average cell-shedding rates become about the same (Fig. 5 *A*). Increasing cell movement toward the shedding sites decreases the average total cell numbers (Fig. 5 *B*), average cell density (Fig. 5 *C*), and average shedding-cell ages (Fig. 5 *D*). Cell density increases toward the shedding sites as α increases (Fig. S5 *A*), which is similar to the cell-density profiles observed in the upper villus region (22). The decreased cell density near the crypts allows space for cells from the crypts and reduces noise due to displacements by cell proliferation in the crypts (Fig. S5 *B*; Video S3). This, in turn, decreases the CVs of shedding-cell ages for large α, and the Long has smaller CVs than the Short does for all α (Fig. 5 *E*). The differences between the early and late shedding-cell ages also decrease as α increases, and the Long has a narrower range of the shedding-cell ages than the Short does for all α (Fig. 5, *F* and *G*). In addition, the average and early shedding-cell ages of the Long fall slightly below those of the Short as α increases, which would be due to different cell motility between the Long and Short caused by the small difference in cell density depending on the shapes (Fig. 5 *C*). To conclude, active cell migration advances the shedding-cell ages and decreases their spread.

Effects of different material properties of cells

In the 3D model and in the normal configuration of the 2D model, we set parameter values of the spring constant (μ) and drag coefficient (η) to minimize cell rearrangements and achieve coordinated collective cell movements, as observed in the villus surface (7,22). However, different parameter values would alter cell behavior and affect shedding-cell age distributions. In the cell-based models, a parameter $\lambda = \mu/\eta$ relates to relaxation timescales at cellular levels (36) and collective cellular diffusion at tissue levels (31,37); a large value of λ corresponds with a short relaxation time and fast and long-distance propagation of internal stress. Here, we simulate the 2D model by fixing $\eta = 1.0$ and varying μ between 10 and 50 to examine the effects on cell turnover with different material states of cells. The settings of the normal configuration are used for the other parameter values except for the crypt depth.

The proliferation rates are set to be equal for all conditions, and the average cell-shedding rates are approximately the same (Fig. 6 *A*). The average total cell numbers (Fig. 6 *B*), average cell density (Fig. 6 *C*), and average shedding-cell ages (Fig. 6 *D*) decrease as λ increases. The cells crowd and move slowly with small λ, and they become sparse and move quickly for large λ (Video S4). Cells are densely packed near the crypts, which leads to a marked

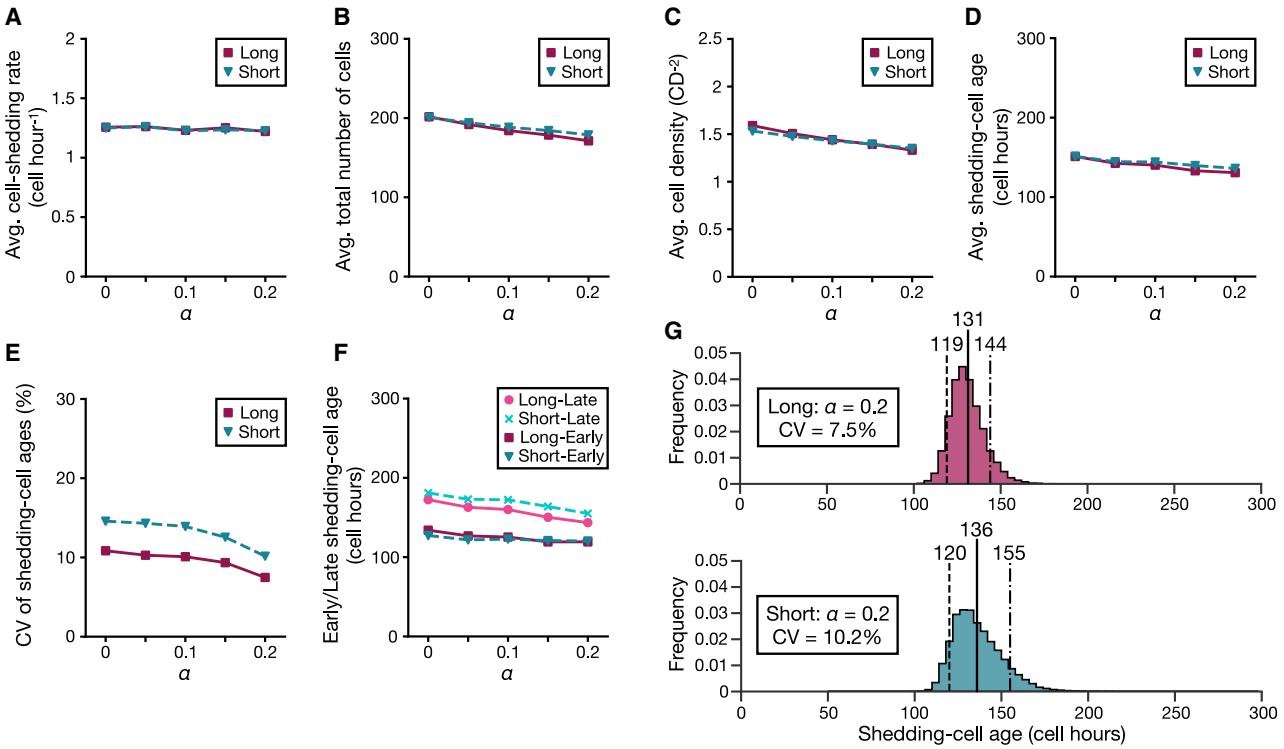

FIGURE 5 Effects of active cell migration. The setting $\alpha = 0$ gives the same outcome as the "normal" results. (*A*) Given is the average number of cells that shed per one cell hour. (*B*) Given is the average total number of cells in the models. (*C*) Given is the average cell density of the models. (*D*) Given is the average shedding-cell age. (*E*) Given is the CV of the shedding-cell ages. (*F*) Given are the early or late shedding-cell ages. (*G*) Shown are the shedding-cell age distributions of the Long (*top*) and Short (*bottom*) for $\alpha = 0.2$. The dashed lines represent the early shedding-cell ages, the solid lines represent the average shedding-cell ages, and the dot-dash lines represent the late shedding-cell ages. To see this figure in color, go online.

decrease in cell density from the crypts to the shedding sites for small λ, and the density approaches uniform for large λ (Fig. S6 *A*). The CVs of the shedding-cell ages show a tendency to increase as λ increases, and the Long has smaller CVs than the Short does for all λ (Fig. 6 *E*). The differences between the early and late shedding-cell ages are the smallest when $\lambda = 30$, and the Long has a narrower range of the shedding-cell ages than the Short for all λ (Fig. 6 *F*). In addition, as in the case of active cell migration, the slight differences in the average shedding-cell ages between the Long and Short would be attributed to different cell motility caused by their cell-density differences (Fig. 6 *C*). For large values of λ, young and old cells mix in the surfaces (Fig. S6 *D*), which would be due to the low cell density and effective propagation of cell-division-driven displacements, thus the shedding-cell ages are widely distributed (Figs. 6 *G* and S6 *B*). By contrast, small λ has gradual cell age distributions with little cell mixing in the surfaces (Fig. S6 *D*), which would be due to the short crypt depth (Table S2) and short-distance propagation of internal stress. However, small λ exhibits bimodal shedding-cell age distributions (Figs. 6 *H* and S6 *C*), which would be due to slight separation of population movement for wide channels caused by the high cell density and slow transportation of internal forces. This is supported by the results that a narrow channel shows a unimodal shedding-cell age distribution (see Supporting materials and methods, Appendix S8; Fig. S6 *E*; Video S5). When $\lambda = 30$, cells distribute within the surfaces in order of age (Fig. S6 *D*), and the shedding-cell ages do not exhibit dual modes (Fig. 4 *D*). Finally, large or small values of λ show wide and multimodal distributions of the shedding-cell ages under the same cell proliferation rates and the same model shapes; a moderate value of λ (=30) leads to coordinated collective cell migration and supports the stochastic model predictions.

DISCUSSION

The villi contribute most of the intestine's luminal surface, which is essential for efficient absorption. Moreover, cell turnover renews the epithelial cells, maintaining the absorption and protection of the small intestine. Although both the villi and cell turnover are crucial for the physiology of the small intestine, how the villi affect cell turnover has not been well investigated. In this study, we used three mathematical models—the stochastic model, the 3D surface cell-based model, and the 2D plane cell-based model—to theoretically propose that the finger-like shape of the villus contributes to the tight regulation of cell turnover. We first presented a stochastic model that focuses on the duration

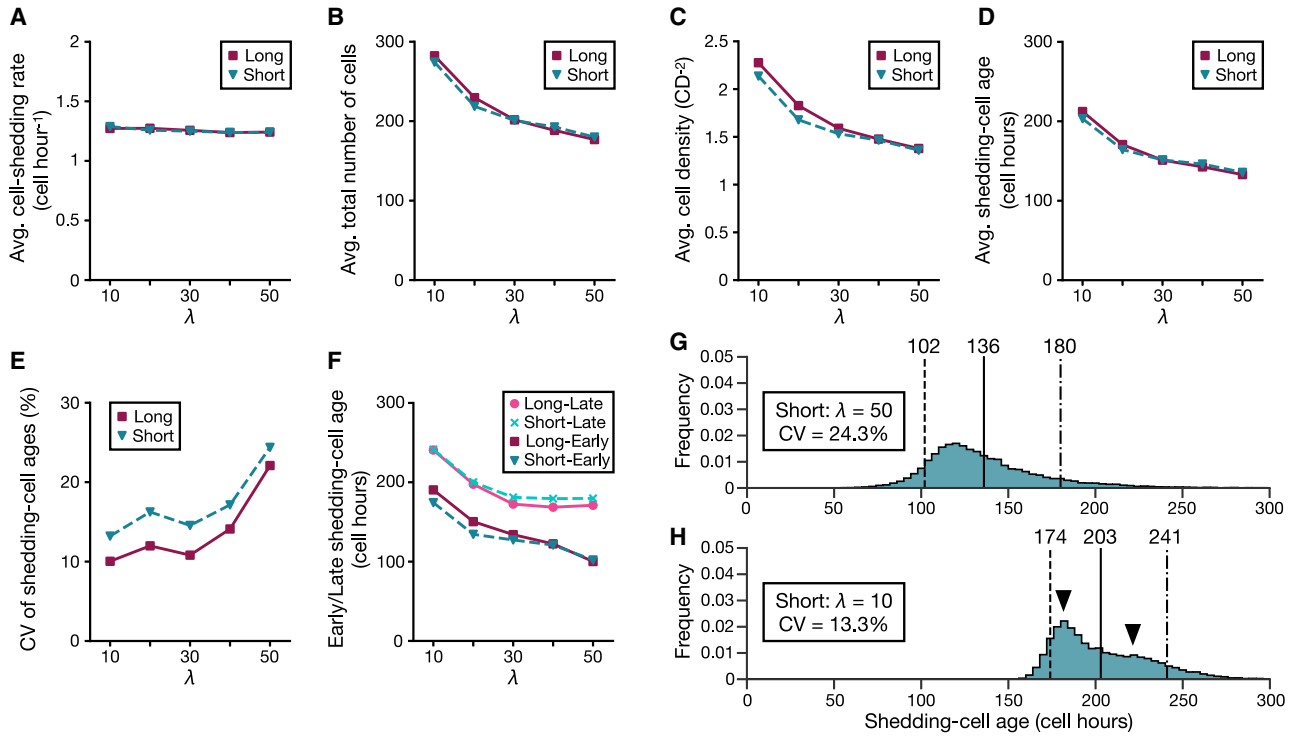

FIGURE 6 Effects of different material properties of cells. The results when $\lambda = 30$ are the same as the "normal" results. (*A*) Given is the average number of cells that shed per one cell hour. (*B*) Given is the average total number of cells in the models. (*C*) Given is the average cell density of the models. (*D*) Given is the average shedding-cell age. (*E*) Given is the CV of the shedding-cell ages. (*F*) Given are the early or late shedding-cell ages. (*G* and *H*) Shown are the shedding-cell age distributions of the Short for $\lambda = 50$ (*G*) and $\lambda = 10$ (*H*). The dashed lines represent the early shedding-cell ages, the solid lines represent the average shedding-cell ages, and the dot-dash lines represent the late shedding-cell ages. Arrowheads indicate the dual modes of the distribution. To see this figure in color, go online.

over which cells migrate the shortest paths between the crypt orifices and the shedding sites. We suggested that tall or pointed villi both lengthen the length of the shortest path and extend its cell migration time, which reduces the spread of shedding-cell ages. We also predicted that compared with the hemispheric and circular disk structures, the finger-like structure has a longer shortest path, and thereby a longer cell migration time, and exhibits a narrower range of shedding-cell ages (Fig. 2 *A*). We then performed simulations of a 3D model for three geometries—Villus, Bump, and Disk—and obtained results similar to those predicted from the stochastic model: the Villus has a narrower range of shedding-cell ages, older early shedding-cell ages, and younger late shedding-cell ages than both the Bump and Disk (Fig. 3 *D*). Lastly, we conducted 2D model simulations for various mechanical conditions of cells. Active migration forces further advance the shedding-cell ages and reduce their spread (Fig. 5), suggesting that the active cell migration promotes cell turnover. We also showed that the shedding-cell age distributions are varied depending on the values of λ (Fig. 6) and that coordinated collective cell migration supports the predictions of the stochastic model.

We examined the effects of the villus height on cell turnover by the stochastic model. The villus height, for instance, differs among the sites of the small intestine in vivo (7): the duodenum has the tallest villi, followed by the jejunum and ileum, in that order. We also explored the effects of the geometrical difference on cell turnover using the hemispheric or circular disk structures (Fig. 1, *B* and *C*). For example, collective cell movement on a hemispheric surface is observed in the retina of teleost fish (38,39); cells from a ring-shaped stem-cell niche in the retinal periphery migrate collectively to the posterior side, which expands the eye size. In addition, cell movement on a circular disk structure is observed in the lobulus hepatis (40); cells produced near the portal triad in the lobular margin move toward the central vein during cell turnover. Observations of cell movement on tissues with different shapes would allow us to further explore the effects of surface shapes on cell turnover. Next, because the stochastic model focuses on the time over which cells move from the origin to their destination, it can be applied to various tissues with collective cell migration. The skin epidermis, for instance, grows from a single layer of proliferative cells at the base (41). Cells divide, differentiate, move outward, and shed from the skin surface. Epidermal cells of about the same age are placed side by side and shed about the same time, suggesting that the shortest-path cell migration times are close to the mean shedding-cell ages, and therefore, the spread of shedding-cell ages would be small (Eq. 7). Branch-like structures are observed

in the epithelium of the lung, kidney, and mammary gland, and cells migrate collectively toward their tips during their morphogenesis (42). If their shapes are symmetric, that is all branches have equal lengths, we would obtain unimodal age distributions of cells reaching the tips of the branches. If they are asymmetric, that is branches differ in their length, there would be multiple shortest-path cell migration times, and the age of cells reaching the tips of the branches would be distributed multimodally. On the other hand, the stomach and large intestine have only randomly arranged crypts in their luminal surfaces, and cells proliferated in the crypts are considered to shed at the crypt orifices or luminal surfaces by anoikis (43,44), making it difficult to identify the shedding sites. Computational simulations would be useful to examine the shedding-cell age distributions of these tissues; the implementation of cell removal depending on cell-basal-membrane distances (45) or local cell density would not require identifying the shedding sites beforehand.

Although we used the cell migration speed, cell density, and cell-shedding rates that are independent of the height or shape of the structures in the stochastic model, they can vary with geometrical features or cell motility. First, experimental studies have indicated that geometrical constraints change collective cell behavior in vitro (46,47); cell populations move faster and more orderly in narrower geometries. Thus, strong geometrical constraints imposed by the thin shape of the villus would increase cell migration speed and lead to coordinated collective cell movement in the villus epithelium. Next, the cell-based models showed that the average cell density varies depending on the surface shapes (Figs. S3 *B* and S4 *D*), suggesting that the total cell numbers differ among structures with the same epithelial surface area. Then, the shedding-cell numbers are suggested to change with the local cell density in anoikis (48); higher cell density promotes cell shedding to maintain homeostatic cell numbers. Because cell shedding at the villus tips is considered to occur by anoikis (23,34), an increase in cell density in the upper villus region due to active cell migration (Fig. S5 *A*; (22)) would promote cell shedding. Finally, it has been suggested that cell extrusion frequency relates to inherent mechanical instability depending on the local curvature of the epithelium (49–51). Tight curvature of the villus tips would hence confer an advantage for cell shedding over flat surfaces, which would further promote cell shedding on the villus. These facts indicate that surface shapes, cell density, and cell behavior are involved in the regulation of cell turnover. In addition, the shortest-path cell migration times, the total cell numbers in the epithelium, and the cell supply and shedding rates would change among structures, and they would be related to each other; e.g., the shortest-path cell migration times would decrease, and the total cell numbers would increase as the cell supply and shedding rates increased. Furthermore, the stochastic model considers graded distributions of cell age in the epithelium, and the cell-based models owe cell-positional fluctuation only to cell division in the crypts. It has been indicated that cell-positional noise affects tissue renewal dynamics depending on the noise sources (52). The implementation of cell age fluctuation in our stochastic model and that of random or directional active cell motility in mechanical models would allow us to understand the effects of cell-positional exchange on cell turnover. Finally, the results of the cell-based models indicate that the material states of cells alter cell population behavior and affect shedding-cell age distributions (Fig. 6). Cellular mechanical properties such as cell stiffness are varied depending on the types or malignancy of cells (53), which would lead to different dynamics of cell turnover.

CONCLUSIONS

We have shown theoretical evidence that the finger-like shape of the villus contributes substantially to the tight regulation of cell turnover in the small intestine and have highlighted the significant roles of the villi in homeostatic maintenance of the small intestine. Our stochastic model suggested that the villus extends the cell migration time over the shortest path between the crypt orifices and the villus tips and decreases the spread of shedding-cell ages. Cell-based dynamic models supported the predictions of the stochastic model and indicated that collective cell behavior also affects the shedding-cell age distributions. Finally, based on the results in this study, we provide two predictions about the influences of the villi on pathophysiology of the small intestine. First, villous atrophy associated with inflammatory diseases (5) would disturb tightly regulated cell turnover maintained by the villi and allow inefficient old cells to remain longer in the intestinal epithelium, which exacerbates malabsorption. Second, compared with other digestive organs, the small intestine has overwhelmingly low risks of tumorigenesis and cancer metastasis from other malignancies (54,55). We suggest that the tight regulation of cell shedding by the villi decreases these risks by reducing old, mutable cells and by shedding mutant cells before their colonization of the intestinal epithelium. We expect that our study would help to explore physiological functions and disorders of the digestive organs, and our approach presented here would be useful to further understand various biological tissues with collective cell movement.

SUPPORTING MATERIAL

Supporting material can be found online at https://doi.org/10.1016/j.bpj.2021.01.003.

AUTHOR CONTRIBUTIONS

Y.K. performed the research and wrote the article.

ACKNOWLEDGMENTS

The author is grateful to Toshiki Oguma and Professor Takashi Miura for their helpful suggestions and continued support. The author also wishes

to thank the anonymous reviewers for their insightful comments on earlier versions of the manuscript.

REFERENCES

1. Cheng, H., and C. P. Leblond. 1974. Origin, differentiation and renewal of the four main epithelial cell types in the mouse small intestine. I. Columnar cell. *Am. J. Anat.* 141:461–479.
2. Hasan, M., and A. Ferguson. 1981. Measurements of intestinal villi non-specific and ulcer-associated duodenitis-correlation between area of microdissected villus and villus epithelial cell count. *J. Clin. Pathol.* 34:1181–1186.
3. Wright, N. A., J. Carter, and M. Irwin. 1989. The measurement of villus cell population size in the mouse small intestine in normal and abnormal states: a comparison of absolute measurements with morphometric estimators in sectioned immersion-fixed material. *Cell Tissue Kinet.* 22:425–450.
4. Helander, H. F., and L. Fändriks. 2014. Surface area of the digestive tract - revisited. *Scand. J. Gastroenterol.* 49:681–689.
5. Macdonald, T. T., and G. Monteleone. 2005. Immunity, inflammation, and allergy in the gut. *Science.* 307:1920–1925.
6. Pearson, A. D., E. J. Eastham, …, R. Nelson. 1982. Intestinal permeability in children with Crohn's disease and coeliac disease. *Br. Med. J. (Clin. Res.).* 285:20–21.
7. Creamer, B., R. G. Shorter, and J. Bamforth. 1961. The turnover and shedding of epithelial cells. I. The turnover in the gastro-intestinal tract. *Gut.* 2:110–118.
8. van der Flier, L. G., and H. Clevers. 2009. Stem cells, self-renewal, and differentiation in the intestinal epithelium. *Annu. Rev. Physiol.* 71:241–260.
9. Darwich, A. S., U. Aslam, …, A. Rostami-Hodjegan. 2014. Meta-analysis of the turnover of intestinal epithelia in preclinical animal species and humans. *Drug Metab. Dispos.* 42:2016–2022.
10. Al-Dewachi, H. S., N. A. Wright, …, A. J. Watson. 1975. Cell population kinetics in the mouse jejunal crypt. *Virchows Arch. B Cell Pathol. Incl. Mol. Pathol.* 18:225–242.
11. Schepers, A. G., R. Vries, …, H. Clevers. 2011. Lgr5 intestinal stem cells have high telomerase activity and randomly segregate their chromosomes. *EMBO J.* 30:1104–1109.
12. Wright, N. A., and M. Irwin. 1982. The kinetics of villus cell populations in the mouse small intestine. I. Normal villi: the steady state requirement. *Cell Tissue Kinet.* 15:595–609.
13. Peterson, L. W., and D. Artis. 2014. Intestinal epithelial cells: regulators of barrier function and immune homeostasis. *Nat. Rev. Immunol.* 14:141–153.
14. Snippert, H. J., L. G. van der Flier, …, H. Clevers. 2010. Intestinal crypt homeostasis results from neutral competition between symmetrically dividing Lgr5 stem cells. *Cell.* 143:134–144.
15. Wong, S. Y., K. H. Chiam, …, P. Matsudaira. 2010. Computational model of cell positioning: directed and collective migration in the intestinal crypt epithelium. *J. R. Soc. Interface.* 7 (*Suppl 3*):S351–S363.
16. Buske, P., J. Galle, …, M. Loeffler. 2011. A comprehensive model of the spatio-temporal stem cell and tissue organisation in the intestinal crypt. *PLoS Comput. Biol.* 7:e1001045.
17. Du, H., Q. Nie, and W. R. Holmes. 2015. The interplay between Wnt mediated expansion and negative regulation of growth promotes robust intestinal crypt structure and homeostasis. *PLoS Comput. Biol.* 11:e1004285.
18. Maclaren, O. J., A. Parker, …, P. K. Maini. 2017. A hierarchical Bayesian model for understanding the spatiotemporal dynamics of the intestinal epithelium. *PLoS Comput. Biol.* 13:e1005688.
19. Kaur, P., and C. S. Potten. 1986. Cell migration velocities in the crypts of the small intestine after cytotoxic insult are not dependent on mitotic activity. *Cell Tissue Kinet.* 19:601–610.
20. Heath, J. P. 1996. Epithelial cell migration in the intestine. *Cell Biol. Int.* 20:139–146.
21. Parker, A., O. J. Maclaren, …, C. Pin. 2017. Cell proliferation within small intestinal crypts is the principal driving force for cell migration on villi. *FASEB J.* 31:636–649.
22. Krndija, D., F. El Marjou, …, D. Matic Vignjevic. 2019. Active cell migration is critical for steady-state epithelial turnover in the gut. *Science.* 365:705–710.
23. Bullen, T. F., S. Forrest, …, A. J. Watson. 2006. Characterization of epithelial cell shedding from human small intestine. *Lab. Invest.* 86:1052–1063.
24. Guan, Y., A. J. Watson, …, M. H. Montrose. 2011. Redistribution of the tight junction protein ZO-1 during physiological shedding of mouse intestinal epithelial cells. *Am. J. Physiol. Cell Physiol.* 300:C1404–C1414.
25. Muraro, D., A. Parker, …, H. M. Byrne. 2018. Chronic TNFα-driven injury delays cell migration to villi in the intestinal epithelium. *J. R. Soc. Interface.* 15:20180037.
26. Parker, A., L. Vaux, …, C. Pin. 2019. Elevated apoptosis impairs epithelial cell turnover and shortens villi in TNF-driven intestinal inflammation. *Cell Death Dis.* 10:108.
27. Mirams, G. R., C. J. Arthurs, …, D. J. Gavaghan. 2013. Chaste: an open source C++ library for computational physiology and biology. *PLoS Comput. Biol.* 9:e1002970.
28. Cheng, H., and M. Bjerknes. 1985. Whole population cell kinetics and postnatal development of the mouse intestinal epithelium. *Anat. Rec.* 211:420–426.
29. Meineke, F. A., C. S. Potten, and M. Loeffler. 2001. Cell migration and organization in the intestinal crypt using a lattice-free model. *Cell Prolif.* 34:253–266.
30. van Leeuwen, I. M., G. R. Mirams, …, H. M. Byrne. 2009. An integrative computational model for intestinal tissue renewal. *Cell Prolif.* 42:617–636.
31. Murray, P. J., C. M. Edwards, …, P. K. Maini. 2009. From a discrete to a continuum model of cell dynamics in one dimension. *Phys. Rev. E Stat. Nonlin. Soft Matter Phys.* 80:031912.
32. Dunn, S. J., I. S. Näthke, and J. M. Osborne. 2013. Computational models reveal a passive mechanism for cell migration in the crypt. *PLoS One.* 8:e80516.
33. Fletcher, A. G., J. M. Osborne, …, D. J. Gavaghan. 2013. Implementing vertex dynamics models of cell populations in biology within a consistent computational framework. *Prog. Biophys. Mol. Biol.* 113:299–326.
34. Williams, J. M., C. A. Duckworth, …, D. M. Pritchard. 2015. Epithelial cell shedding and barrier function: a matter of life and death at the small intestinal villus tip. *Vet. Pathol.* 52:445–455.
35. Tsubouchi, S. 1983. Theoretical implications for cell migration through the crypt and the villus of labelling studies conducted at each position within the crypt. *Cell Tissue Kinet.* 16:441–456.
36. Mathias, S., A. Coulier, …, A. Hellander. 2020. Impact of force function formulations on the numerical simulation of centre-based models. *Bull. Math. Biol.* 82:132.
37. Murray, P. J., A. Walter, …, P. K. Maini. 2011. Comparing a discrete and continuum model of the intestinal crypt. *Phys. Biol.* 8:026011.
38. Centanin, L., B. Hoeckendorf, and J. Wittbrodt. 2011. Fate restriction and multipotency in retinal stem cells. *Cell Stem Cell.* 9:553–562.
39. Tsingos, E., B. Höckendorf, …, J. Wittbrodt. 2019. Retinal stem cells modulate proliferative parameters to coordinate post-embryonic morphogenesis in the eye of fish. *eLife.* 8:e42646.
40. Zajicek, G., R. Oren, and M. Weinreb, Jr. 1985. The streaming liver. *Liver.* 5:293–300.
41. Fuchs, E. 2008. Skin stem cells: rising to the surface. *J. Cell Biol.* 180:273–284.
42. Wang, S., R. Sekiguchi, …, K. M. Yamada. 2017. Patterned cell and matrix dynamics in branching morphogenesis. *J. Cell Biol.* 216:559–570.

43. Gavrieli, Y., Y. Sherman, and S. A. Ben-Sasson. 1992. Identification of programmed cell death in situ via specific labeling of nuclear DNA fragmentation. *J. Cell Biol.* 119:493–501.

44. Windham, T. C., N. U. Parikh, …, G. E. Gallick. 2002. Src activation regulates anoikis in human colon tumor cell lines. *Oncogene*. 21:7797–7807.

45. Ingham-Dempster, T. A., R. Rosser, …, D. C. Walker. 2020. From cell to multi-crypt: agent-based models of the human colon suggests novel processes of Field cancerisation. *J. Comput. Sci.* 41:101066.

46. Vedula, S. R. K., M. C. Leong, …, B. Ladoux. 2012. Emerging modes of collective cell migration induced by geometrical constraints. *Proc. Natl. Acad. Sci. USA*. 109:12974–12979.

47. Yevick, H. G., G. Duclos, …, P. Silberzan. 2015. Architecture and migration of an epithelium on a cylindrical wire. *Proc. Natl. Acad. Sci. USA*. 112:5944–5949.

48. Eisenhoffer, G. T., P. D. Loftus, …, J. Rosenblatt. 2012. Crowding induces live cell extrusion to maintain homeostatic cell numbers in epithelia. *Nature*. 484:546–549.

49. Okuda, S., and K. Fujimoto. 2020. A mechanical instability in planar epithelial monolayers leads to cell extrusion. *Biophys. J.* 118:2549–2560.

50. Hannezo, E., J. Prost, and J. F. Joanny. 2011. Instabilities of monolayered epithelia: shape and structure of villi and crypts. *Phys. Rev. Lett.* 107:078104.

51. Maechler, F. A., C. Allier, …, C. Tomba. 2019. Curvature-dependent constraints drive remodeling of epithelia. *J. Cell Sci.* 132:jcs222372.

52. Corominas-Murtra, B., C. L. G. J. Scheele, …, E. Hannezo. 2020. Stem cell lineage survival as a noisy competition for niche access. *Proc. Natl. Acad. Sci. USA*. 117:16969–16975.

53. Guck, J., S. Schinkinger, …, C. Bilby. 2005. Optical deformability as an inherent cell marker for testing malignant transformation and metastatic competence. *Biophys. J.* 88:3689–3698.

54. Lowenfels, A. B. 1973. Why are small-bowel tumours so rare? *Lancet.* 1:24–26.

55. Dabaja, B. S., D. Suki, …, J. Ajani. 2004. Adenocarcinoma of the small bowel: presentation, prognostic factors, and outcome of 217 patients. *Cancer.* 101:518–526.

Biophysical Journal, Volume *120*

Supplemental Information

Intestinal villus structure contributes to even shedding of epithelial cells

Yuto Kai

Supporting Material for Intestinal Villus Structure Contributes to Even Shedding of Epithelial Cells

Appendix S1: Derivation of the expected value and standard deviation of the shedding-cell ages

Let X be the stochastic variable representing the age when cells shed. First, the expected value of the shedding-cell age of the finger-like villus is given by

$$E(X) = \sum_{t=\tau_\mathrm{f}+1}^{\infty} t p_\mathrm{f} (1-p_\mathrm{f})^{t-\tau_\mathrm{f}-1}. \tag{S1}$$

By putting $k = t - \tau_\mathrm{f}$, we have

$$\begin{aligned} E(X) &= \sum_{k=1}^{\infty} (k+\tau_\mathrm{f}) p_\mathrm{f} (1-p_\mathrm{f})^{k-1} \\ &= p_\mathrm{f} \left[(1+\tau_\mathrm{f})(1-p_\mathrm{f})^0 + (2+\tau_\mathrm{f})(1-p_\mathrm{f})^1 + \cdots \right]. \end{aligned} \tag{S2}$$

Next, multiplying the both sides of Eq. S2 by $(1-p_\mathrm{f})$, we calculate

$$\begin{aligned} E(X) - (1-p_\mathrm{f})E(X) &= p_\mathrm{f} \left[\tau_\mathrm{f} + (1-p_\mathrm{f})^0 + (1-p_\mathrm{f})^1 + \cdots \right] \\ &= p_\mathrm{f} \left[\tau_\mathrm{f} + \frac{1}{1-(1-p_\mathrm{f})} \right]. \end{aligned} \tag{S3}$$

Finally, substituting $p_\mathrm{f} = n/(N - n\tau_\mathrm{f})$ from Eq. 5 into Eq. S3, the expected value is solved as

$$E(X) = \tau_\mathrm{f} + \frac{1}{p_\mathrm{f}} = \frac{N}{n} = T. \tag{S4}$$

To derive the standard deviation (SD) of the shedding-cell ages of the finger-like villus, we begin by calculating

$$E(X^2) = \sum_{t=\tau_\mathrm{f}+1}^{\infty} t^2 p_\mathrm{f} (1-p_\mathrm{f})^{t-\tau_\mathrm{f}-1}. \tag{S5}$$

Putting $k = t - \tau_\mathrm{f}$, we have

$$\begin{aligned} E(X^2) &= \sum_{k=1}^{\infty} (k+\tau_\mathrm{f})^2 p_\mathrm{f} (1-p_\mathrm{f})^{k-1} \\ &= p_\mathrm{f} \left[(1+\tau_\mathrm{f})^2 (1-p_\mathrm{f})^0 + (2+\tau_\mathrm{f})^2 (1-p_\mathrm{f})^1 + \cdots \right]. \end{aligned} \tag{S6}$$

Next, multiplying the both sides of Eq. S6 by $(1-p_\mathrm{f})$, we calculate

$$E(X^2) - (1-p_\mathrm{f})E(X^2) = p_\mathrm{f} \left[\{(1+\tau_\mathrm{f})^2 - 0^2\}(1-p_\mathrm{f})^0 + \{(2+\tau_\mathrm{f})^2 - (1+\tau_\mathrm{f})^2\}(1-p_\mathrm{f})^1 + \cdots \right], \tag{S7}$$

and get

$$E(X^2) = \tau_\mathrm{f}^2 + \left[(1+2\tau_\mathrm{f})(1-p_\mathrm{f})^0 + (3+2\tau_\mathrm{f})(1-p_\mathrm{f})^1 + \cdots \right]. \tag{S8}$$

Multiply the both sides of Eq. S8 by $(1-p_\mathrm{f})$ again, and we calculate

$$\begin{aligned} E(X^2) - (1-p_\mathrm{f})E(X^2) &= \tau_\mathrm{f}^2 - (1-p_\mathrm{f})\tau_\mathrm{f}^2 + \left[(1+2\tau_\mathrm{f})(1-p_\mathrm{f})^0 + 2(1-p_\mathrm{f})^1 + 2(1-p_\mathrm{f})^2 + \cdots \right] \\ &= p_\mathrm{f}\tau_\mathrm{f}^2 + \frac{2p_\mathrm{f}\tau_\mathrm{f} - p_\mathrm{f} + 2}{p_\mathrm{f}}, \end{aligned} \tag{S9}$$

and obtain

$$E(X^2) = \tau_\mathrm{f}^2 + \frac{2p_\mathrm{f}\tau_\mathrm{f} - p_\mathrm{f} + 2}{p_\mathrm{f}^2}. \tag{S10}$$

The variance of the shedding-cell ages is calculated from Eqs. S4 and S10 as

$$\begin{aligned} V(X) &= E(X^2) - [E(X)]^2 \\ &= \tau_{\mathrm{f}}^2 + \frac{2p_{\mathrm{f}}\tau_{\mathrm{f}} - p_{\mathrm{f}} + 2}{p_{\mathrm{f}}^2} - \left(\tau_{\mathrm{f}} + \frac{1}{p_{\mathrm{f}}}\right)^2 \\ &= \frac{1 - p_{\mathrm{f}}}{p_{\mathrm{f}}^2}, \end{aligned} \tag{S11}$$

thus the SD of the shedding-cell ages is given by

$$\sigma_{\mathrm{f}} = \frac{\sqrt{1 - p_{\mathrm{f}}}}{p_{\mathrm{f}}}. \tag{S12}$$

Finally, substituting $p_{\mathrm{f}} = n/(N - n\tau_{\mathrm{f}})$ from Eq. 5 into Eq. S12 and using $T = N/n$ from Eq. S4, we obtain

$$\sigma_{\mathrm{f}} = \sqrt{(T - \tau_{\mathrm{f}})(T - \tau_{\mathrm{f}} - 1)}. \tag{S13}$$

Appendix S2: Effects of the height of the finger-like villus

In this section, we examine how the height of the finger-like villus affects the spread of shedding-cell ages in the stochastic model. As shown in Fig. S1A, let r be the radius of the hemisphere and cylinder and h be the height of the cylinder of the finger-like structure. The length of the shortest path between the crypt orifices and the tip of the finger-like structure is

$$L_{\mathrm{f}} = \frac{1}{2}\pi r + h, \tag{S14}$$

and the epithelial surface area of the finger-like structure is

$$S_{\mathrm{f}} = 2\pi r^2 + 2\pi r h = 2\pi r(r + h). \tag{S15}$$

The cylinder base is not part of the epithelial surface area. From Eqs. S14 and S15, we obtain

$$L_{\mathrm{f}} = \frac{1}{4}\sqrt{2\pi S_{\mathrm{f}} + \pi^2 h^2} + \left(1 - \frac{\pi}{4}\right) h, \tag{S16}$$

and using Eq. S15, the overall height of the finger-like structure can be expressed in terms of its surface area as

$$H_{\mathrm{f}} = r + h = \frac{1}{2}\sqrt{\frac{2S_{\mathrm{f}}}{\pi} + h^2} + \frac{h}{2}. \tag{S17}$$

Thus, when S_{f} is constant, L_{f} increases as H_{f} increases via h, that is, the length of the shortest path between the crypt orifices and the villus tip lengthens as the overall height of the finger-like structure increases. Assuming that the cell migration speed is independent of the villus height, τ_{f} also increases as L_{f} increases. Assuming that the cell density is independent of the villus height, N is constant when the epithelial surface areas are the same. We also assume that n is the same regardless of the villus height. Therefore, although T is the same from Eq. S4, σ_{f} decreases as τ_{f} increases (Eq. S13) when $\tau_{\mathrm{f}} < T$ is established. A taller finger-like villus extends the length of the shortest path between the crypt orifices and the villus tip, and thereby delays the cell migration time over the shortest path, which reduces the spread of shedding-cell ages.

Appendix S3: Comparison of the finger-like and conical structures

In this section, we compare the spread of shedding-cell ages of the finger-like and conical structures using the stochastic model. First, we consider a right conical structure with the same epithelial surface area and radius as the finger-like structure as shown in Fig. S1B. The conical structure is assumed to be surrounded by crypts as with the finger-like structure, and cells move from the base and shed at the tip of the cone. Let r be its radius, l the slant height, and L_{co} the length of the shortest path of the conical structure, i.e., $L_{\mathrm{co}} = l$ (for a right circular cone). Considering an epithelial surface area of the conical structure equal to the finger-like structure, we obtain from Eq. S15

$$l = L_{\mathrm{co}} = \frac{S_{\mathrm{f}}}{\pi r} = 2(r + h). \tag{S18}$$

Here, the cone base is not part of the epithelial surface area. Again, h is the height of the cylinder of the finger-like structure. Then,

$$L_{\mathrm{co}} - L_{\mathrm{f}} = \left(2 - \frac{\pi}{2}\right) r + h > 0, \tag{S19}$$

that is, $L_{\mathrm{co}} > L_{\mathrm{f}}$ always holds regardless of r and h. We assume that the cell migration speed and cell density are independent of the shape of the structures, and that cell supply and shedding rates are constant regardless of the structures. Both structures hence have the same stochastic processes except for the shortest-path cell migration times. That is, both structures have the same values of N and n, but the conical structure has a longer shortest-path cell migration time than the finger-like structure. Finally, T is the same from Eq. S4, but the conical structure has a smaller SD of the shedding-cell ages than the finger-like structure from Eq. S13, under the condition that the conical structure's shortest-path cell migration time is smaller than T.

Appendix S4: Comparison of the finger-like, hemispheric, and circular disk structures

In this section, we first calculate the lengths of the shortest path between the crypt orifices and the shedding sites of the hemispheric and circular disk structures that have the same epithelial surface areas as the finger-like structure. We then compare the spread of shedding-cell ages among the finger-like, hemispheric, and circular disk structures using the stochastic model.

As shown in Fig. S1C, let ψ be the radius and L_{h} be the length of the shortest path of the hemispheric structure. As shown in Fig. S1D, let R be the radius and L_{c} be the length of the shortest path of the circular disk structure, where $R = L_{\mathrm{c}}$. Considering that both structures have the same epithelial surface area as the finger-like structure, each is expressed from Eq. S15 as

$$\psi = \sqrt{\frac{S_{\mathrm{f}}}{2\pi}} = \sqrt{r(r+h)}, \tag{S20}$$

$$L_{\mathrm{h}} = \frac{1}{2}\pi\psi = \frac{1}{2}\pi\sqrt{r(r+h)}, \tag{S21}$$

and

$$R = L_{\mathrm{c}} = \sqrt{\frac{S_{\mathrm{f}}}{\pi}} = \sqrt{2r(r+h)}. \tag{S22}$$

The base of the hemisphere does not contribute any epithelial surface area. We then compare the lengths of the shortest path among the three structures as follows:

$$L_{\mathrm{f}}^2 - L_{\mathrm{h}}^2 = \left(\pi - \frac{1}{4}\pi^2\right) rh + h^2 > 0, \tag{S23}$$

and

$$L_{\mathrm{h}}^2 - L_{\mathrm{c}}^2 = \left(\frac{1}{4}\pi^2 - 2\right) r^2 + \left(\frac{1}{4}\pi^2 - 2\right) rh > 0, \tag{S24}$$

that is, $L_{\mathrm{f}} > L_{\mathrm{h}} > L_{\mathrm{c}}$ always holds regardless of r and h. Again, we assume that the cell migration speed and cell density are independent of the shape of the structures, and that cell supply and shedding rates are constant regardless of the structures. The shortest cell migration time, therefore, decreases in the same order: $\tau_{\mathrm{f}} > \tau_{\mathrm{h}} > \tau_{\mathrm{c}}$, and all structures have the same values of N and n. The stochastic processes of all structures are the same except for the shortest-path cell migration times (Fig. 1), and the SDs of the shedding-cell ages of the hemispheric or circular disk structures are expressed by replacing τ_{f} of Eq. S13 with τ_{h} or τ_{c}. Finally, although T is the same among structures (Eq. S4), the finger-like structure has the least SDs of the shedding-cell ages, followed by the hemispheric and circular disk structures: $\sigma_{\mathrm{f}} < \sigma_{\mathrm{h}} < \sigma_{\mathrm{c}}$, when $\tau_{\mathrm{f}} < T$ is established. Here, σ_{h} and σ_{c} are the SDs of the shedding-cell ages of the hemispheric and circular disk structures.

Appendix S5: Derivation of the parameter values of the numerical calculation in the stochastic model

We estimate the parameter values of the numerical calculation in the stochastic model mainly based on the results of the experimental study of the murine intestinal villi by Krndija *et al.* (1). First, from a microscopic image of the side elevation of a finger-like villus shown in the study (1), we obtain the radius of the hemisphere and cylinder and height of the cylinder of the finger-like structure as $r = 50\mu$m and $h = 250\mu$m, respectively. We then estimate the length of the shortest path of the finger-like structure as $L_{\mathrm{f}} \sim 328.5\mu$m from Eq. S14 and the epithelial surface area of the finger-like structure as $S_{\mathrm{f}} \sim 94,248\mu\mathrm{m}^2$ from Eq. S15. Next, we

get the average cell density in the villus epithelium as $0.02/\mu\text{m}^2$ from the same villus image calculated by dividing the number of cells by the areas that cells occupy, and estimate the total number of cells in the finger-like structure's epithelial surface as $N = 94,248 \times 0.02 \sim 1,885$. Then, we obtain the average cell migration speed in the epithelium as 5μm/h as measured in the same study (1), and we estimate the shortest-path cell migration duration of the finger-like structure as $\tau_\text{f} = 328.5/5 \sim 65$ hours. Considering the discreteness of the stochastic model, the fractional part is truncated. Finally, the cell supply and shedding rates cannot be directly measured. It has been considered that cells ascend the villus over ~3 days (2), and we choose $n = 26$ hour^{-1} from Eq. S4 so that the average shedding-cell age becomes ~72 hours.

The lengths of the shortest path of the hemispheric and circular disk structures, with equal epithelial surface areas as the finger-like structure, are calculated as $L_\text{h} \sim 192.4\mu$m and $L_\text{c} \sim 173.2\mu$m from Eqs. S21 and S22, respectively. Assuming that both structures have the same average cell velocity as the finger-like structure, the shortest-path cell migration times are estimated as $\tau_\text{h} = 192.4/5 \sim 38$ hours and $\tau_\text{c} = 173.2/5 \sim 34$ hours, respectively. Next, assuming that both structures have the same average cell density in the epithelium as the finger-like structure, both structures also have $N = 1,885$ cells in their epithelial surfaces. In addition, we assume that both structures have the same cell supply and shedding rate $n = 26$ hour^{-1} as the finger-like structure. All structures, therefore, have the same total cell number $N = 1,885$ and cell supply and shedding rate $n = 26$ hour^{-1}, but different cell migration times of the shortest path: $\tau_\text{f} = 65$ hours, $\tau_\text{h} = 38$ hours, or $\tau_\text{c} = 34$ hours.

In the numerical calculation of the stochastic model, we proceed with the calculation loop as follows for each hour: n randomly-selected cells are removed as the shedding cells from those aged over the respective shortest-path cell migration times: τ_f, τ_h, or τ_c; remaining intraepithelial cells increment their age by one hour; we add n cells of age one hour in the epithelium. We put $N = 1,885$ cells of age one hour as an initial state. We run the simulation over 5,000 hours to attain a steady state, and then run for a further 15,000 hours. We obtain the data from the 15,000-hour calculation.

Appendix S6: Evaluation of the numerical calculation results in the stochastic model

In this section, we analytically calculate the SDs of the shedding-cell ages and the average intraepithelial-cell ages, and evaluate the results of the numerical calculation in the stochastic model.

Letting $T = N/n = 1,885/26 = 72.5$ hours from Eq. S4 and $\tau_\text{f} = 65$ hours in Eq. S13, we obtain $\sigma_\text{f} = 7$ hours. Similarly, $\sigma_\text{h} = 34$ hours and $\sigma_\text{c} = 38$ hours. These match the values of the numerical calculation as described in Fig. 2A.

Next, the average intraepithelial-cell age of the finger-like structure is given by

$$\frac{n}{N}\left[\sum_{t=1}^{\tau_\text{f}} t + \sum_{t=\tau_\text{f}+1}^{\infty} t(1-p_\text{f})^{t-\tau_\text{f}-1}\right]. \tag{S25}$$

Letting $N = 1,885$, $n = 26$ hour^{-1}, $\tau_\text{f} = 65$ hours, and $p_\text{f} = 2/15$ from Eq. 5 in Eq. S25, we obtain 37 hours. In the same way, we get 44.7 hours and 46.7 hours for the hemispheric and circular disk structures, respectively. These match the values of the numerical calculation as indicated by solid lines in Fig. 2B.

Appendix S7: Determination of the parameter values and dimensions in the cell-based models

In this section, we provide the determination of parameter values and dimensions in the 3D surface and 2D plane cell-based models. We conducted computational simulations of the cell-based models within Chaste, an open-source C++ library that provides a systematic framework for multi-cellular simulations (3). In both cell-based models, we proceed with the simulation loop as follows for each time step: neighboring cells are identified as having centers within the interaction distance; we calculate forces acting on each cell by Eq. 1; new cell locations are calculated by Eq. 3, and cells reach the shedding sites are removed; cell ages are updated and cell division occurs.

a 3D surface cell-based model

Figure S2 depicts the Villus, Bump and Disk models. All three structures have eight crypts of equal size arranged around regions with circular boundaries. The ratio of the radius to the height of the Villus is 1:5, which is equal to that used in the stochastic model. The Bump is hemispherical, and is wider and shorter than the Villus. In both structures, cells leaving the crypts enter the structures through a sloped base. In the Disk, cells leaving the crypts move directly onto the surface. In all structures, cells passing through the circular boundaries re-enter the regions from the center-symmetric positions to reduce the artificial accumulation of cells at the boundaries. All structures are scaled to have ~600 cells, of which ~150 are proliferating cells and ~450 are differentiated cells. The shedding sites are placed at heights of 14.9 cell diameters (CDs) and 7.535 CDs from the crypt orifices of the Villus and Bump, respectively. The Disk's shedding site, 1.4 CDs in diameter, is at its center. These shedding sites are determined to have

equal perimeters and to provide similar cell-shedding behavior among structures. The length of the shortest path between the crypt orifices and the shedding sites is shorter 17.9 CDs on the Villus, 11.9 CDs on the Bump, and 9.1 CDs on the Disk.

We use spring constant $\mu = 30$ and drag coefficient $\eta = 1.0$ for all structures (3) and confirmed that cells ascend sides of the Villus with little rearrangements (Movie S1). We set 1.5 CDs as the interaction distance between neighboring cells and 1/120 cell hour as the time step Δt (3). The division interval of each proliferative cell is drawn from a truncated normal distribution with mean 10 cell hours, standard deviation 100, and lower band 10 cell hours to ensure that cell division does not artificially synchronize and so the total cell number fluctuates by no more than 5% for all structures (Fig. S3A). All structures are set to have approximately equal numbers of proliferative cells and similar division intervals, with approximately the same proliferation rates among the structures, confirmed by the approximately equal average cell-shedding rates among structures (Fig. 3B). We summarize the parameter values used in the 3D model in Table S1.

In the 3D model simulations, proliferative cells are placed in the crypt surfaces as an initial state. We first calculate 2,000 cell hours to establish until steady-state conditions, and then run further 14,000 cell hours, which is repeated twice. The shedding-cell ages and differentiated-cell ages were obtained for each cell hour. We combine the results of twice-repeated simulations at steady state and obtain data.

b 2D plane cell-based model

In the 2D plane cell-based model, the cell interaction neighborhood radius is 1.5 CDs and the time step Δt is 1/120 cell hour. As normal settings, we use spring constant $\mu = 30$ and drag coefficient $\eta = 1.0$ as in the 3D model. The Long and Short models are depicted in Fig. S4A. Their dimensions are determined based on the "normal" settings that we use in the results of Fig. 4. Both have one crypt and one shedding site, and the widths of the crypt and that of the shedding site are equal between them. We determine the widths and lengths of the shapes based on a cell arrangement where cells are connected by springs of natural length as shown in Fig. S4B. The spacing between cell columns is $\sqrt{3}/2$ CDs as indicated by the red arrow, and we set the width of $7 \times \sqrt{3}/2 \sim 6.06$ CDs for the Long and that of $9 \times \sqrt{3}/2 \sim 7.79$ CDs for the Short so that 8 and 10 cell columns fit within their widths, respectively. We then set the lengths of shapes as indicated by green dotted lines in Fig. S4A for a total cell number of ~200. The crypts and the shedding sites are tapered to the transport regions by straight lines with slopes of ±0.5, which come from the lines connecting adjacent cell centers as indicated by the dotted red lines in Fig. S4B. These taperings are useful for making the influences of the shapes of the Long and Short on cell behavior roughly the same. To reduce artificial cell movement along the boundaries, the periodic boundary condition is imposed on the left- and right-hand sides, as indicated by the red lines of Fig. S4A: cells passing through one side re-enter the regions through the opposite side. Other black lines have the reflective boundary condition. Finally, we confirmed that collective cell migration with little cell rearrangement is achieved in the upper regions of both shapes under the normal settings (Fig. 4A and Movie S2).

We select the cell proliferation rates so that cell shed smoothly and so that fluctuations in the total cell number are below 5% for both shapes (Fig. S4C). The cell proliferation rate is defined by the proliferative-cell number and cell-division interval. For both shapes, the division interval of each proliferative cell is drawn from a truncated normal distribution with mean 8 cell hours, standard deviation 3, and lower band 8 cell hours, which is chosen to ensure that cell division does not artificially synchronize. Next, the Short requires a slightly longer crypt depth (D) to have approximately equal proliferative-cell numbers as the Long, as shown in Table S2, because the Short has a lower average cell density than the Long (Fig. S4D).

In the 2D model, we also examine two cases: active cell migration and different material properties of cells.

Active cell migration. We vary α between 0 and 0.2 where cell proliferation rates and cell-shedding rates can be balanced. We use the parameter values of the normal condition except for D.

Different material properties of cells. We fix $\eta = 1.0$ and vary μ between 10 and 50. We use the parameter values of the normal condition except for μ and D.

In both cases, we use the same model shapes except for D (Fig. S4A). For consistency, we set approximately equal cell proliferation rates for all conditions. To accomplish this, we need to set approximately equal division intervals and proliferative-cell numbers among different conditions. The proliferative-cell density in the crypts also varies because the average cell density varied with the parameter values (Figs. 5C and 6C). We hence regulated D so that all conditions have ~15 proliferative cells in each crypt as shown in Table S2. Finally, all conditions show approximately equal average cell-shedding rates (Figs. 5A and 6A), which ensures approximately equal cell proliferation rates among different conditions.

In the simulations of the 2D model, proliferative cells are placed in the crypt surfaces as an initial state. we first calculate for 1,000 cell hours to establish a steady state, and then run for a further 7,000 cell hours, which is repeated two times. The shedding-cell ages and differentiated-cell ages were obtained for each cell hour. We combine the results of twice-repeated simulations at steady state and obtain data.

Calculation of cell density

In both cell-based models, we divide respective average number of differentiated cells by the surface areas subtracting the crypt surface areas to obtain the average cell density.

In the 3D model, we obtain average cell density profiles of the Villus and Disk as follows: the cylindrical part of the Villus and Disk are divided into five regions as indicated by the dotted red and blue lines as shown in Fig. S2; we divide the average cell number of each region by its surface area; we calculate rescaled average cell density of each region relative to region one.

In the 2D model, we get average cell density profiles of the Long and Short as follows: each model is divided into five regions indicated by the dotted purple and cyan lines as shown in Fig. S4A; the average cell number of each region is divided by its surface area; we calculate rescaled average cell density of each region relative to region one.

Appendix S8: Simulation of the Narrow shape in the 2D plane cell-based model

In this section, we examine whether the width of the model affects the separation of cell population movement for a small value of λ (= 10). We then built a shape with the same length as the Long model but a narrower width, as shown in Fig. S6Ei. The width is chosen so that the average total cell number is ~200 when λ = 10 (Fig. S6Eii); other geometrical parameters are the same as in Fig. S4A. We regulate D and set an equal cell proliferation rate to the normal condition (Table S2), and the average cell-shedding rate becomes approximately the same as the normal (Fig. S6Eiii). Cells move slowly with little cell mixing in the narrow shape (Movie S5), and gradual cell age distribution is shown on the surface (Fig. S6Eiv). As shown in Fig. S6Ev, the narrow shape exhibits a unimodal shedding-cell age distribution, indicating that the separation of population movement does not occur in the narrow channel. Wider channels, therefore, lead the separation of cell population movement, and the threshold width of the separation would depend on the magnitude of λ.

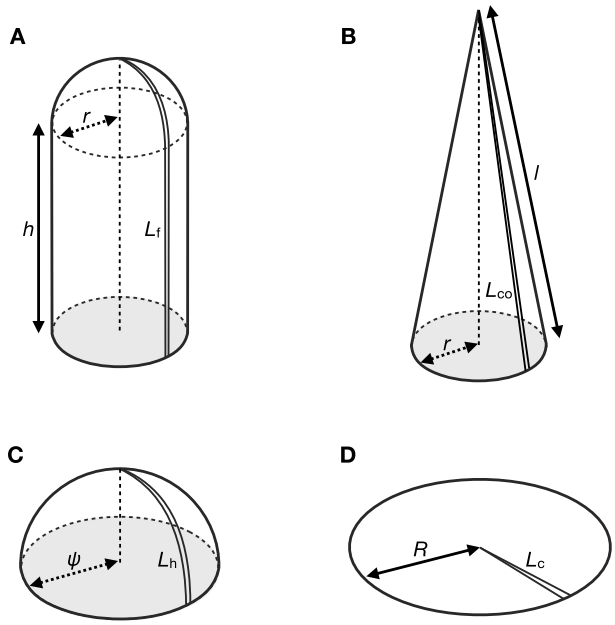

Figure S1: Four structures considered in the stochastic model: the finger-like (A), conical (B), hemispheric (C), and circular disk structures (D). The finger-like, conical, and hemispheric structures do not have their bases that are colored gray: base areas of these structures are not included in the respective epithelial surface areas. (A) The finger-like structure comprises a hemisphere with radius r coupled to a cylinder with radius r and height h. L_f is the length of the shortest path between the crypt orifices and the tip of the finger-like structure. (B) Shown is the conical structure (a right circular cone) with radius r and slant height l. L_{co} is the length of the shortest path between the crypt orifices and the tip of the cone; L_{co} is equal to l. (C) Given is the hemispheric structure with radius ψ. L_h is the length of the shortest path between the crypt orifices and the tip of the hemisphere. (D) Shown is the circular disk structure with radius R. L_c is the length of the shortest path between the crypt orifices and the center of the circle; L_c is equal to R.

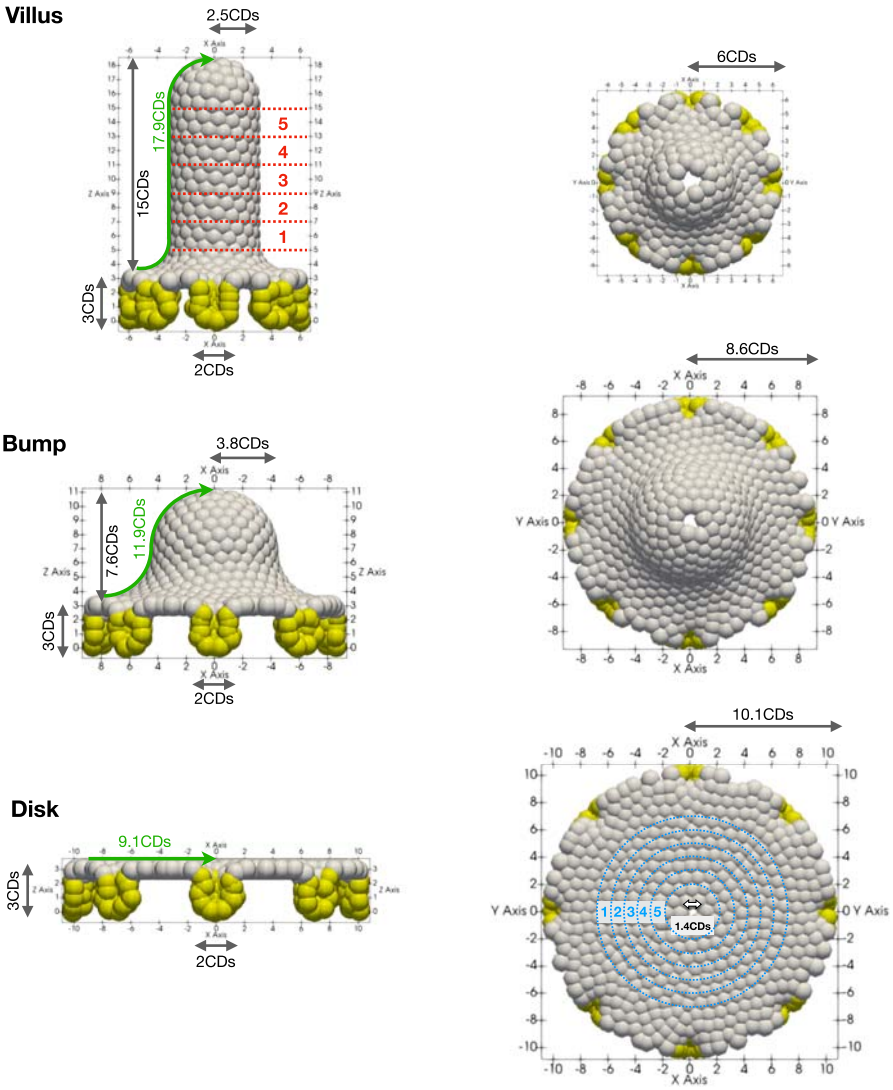

Figure S2: 3D surface cell-based models: Villus (*top*), Bump (*middle*), and Disk (*bottom*). The spatial units are cell diameters (CDs). The left panels are the side elevations and the right panels are the top-down plan views. Proliferative cells are colored yellow; differentiated cells are colored white. Holes seen in the plan views are shedding sites. Green arrows on the elevations show the shortest paths between the crypt orifices and the shedding sites. The red and blue numbers of the Villus and Disk indicate zones for calculating local average cell density.

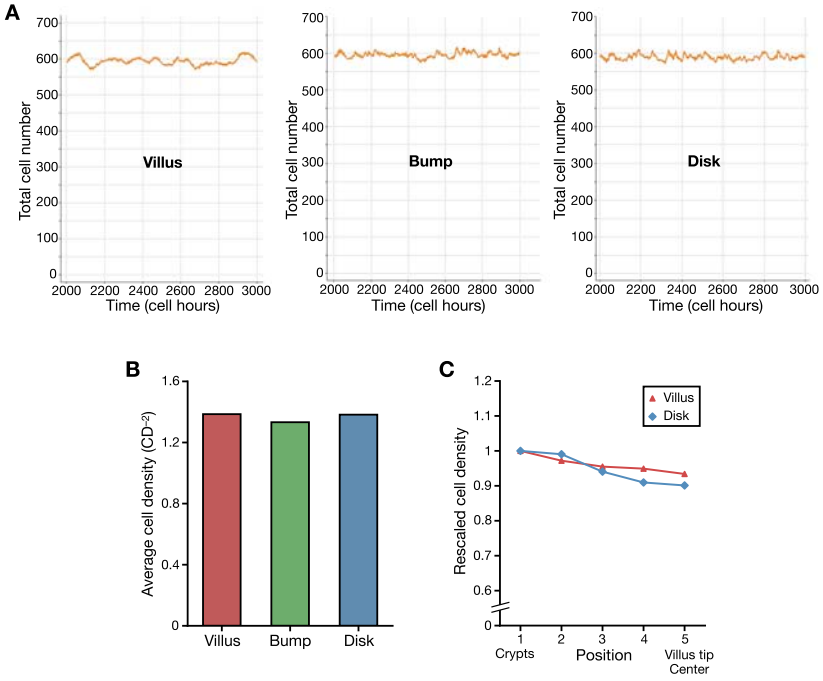

Figure S3: 3D surface cell-based model results. (A) Given are the total cell numbers at steady state of the Villus (*left*), Bump (*middle*), and Disk (*right*). (B) Given is the average cell density. (C) Given are the rescaled average cell density profiles along the crypt–villus tip (Villus) or crypt–center (Disk) axes. Each position number corresponds to a divided zone as shown in Fig. S2.

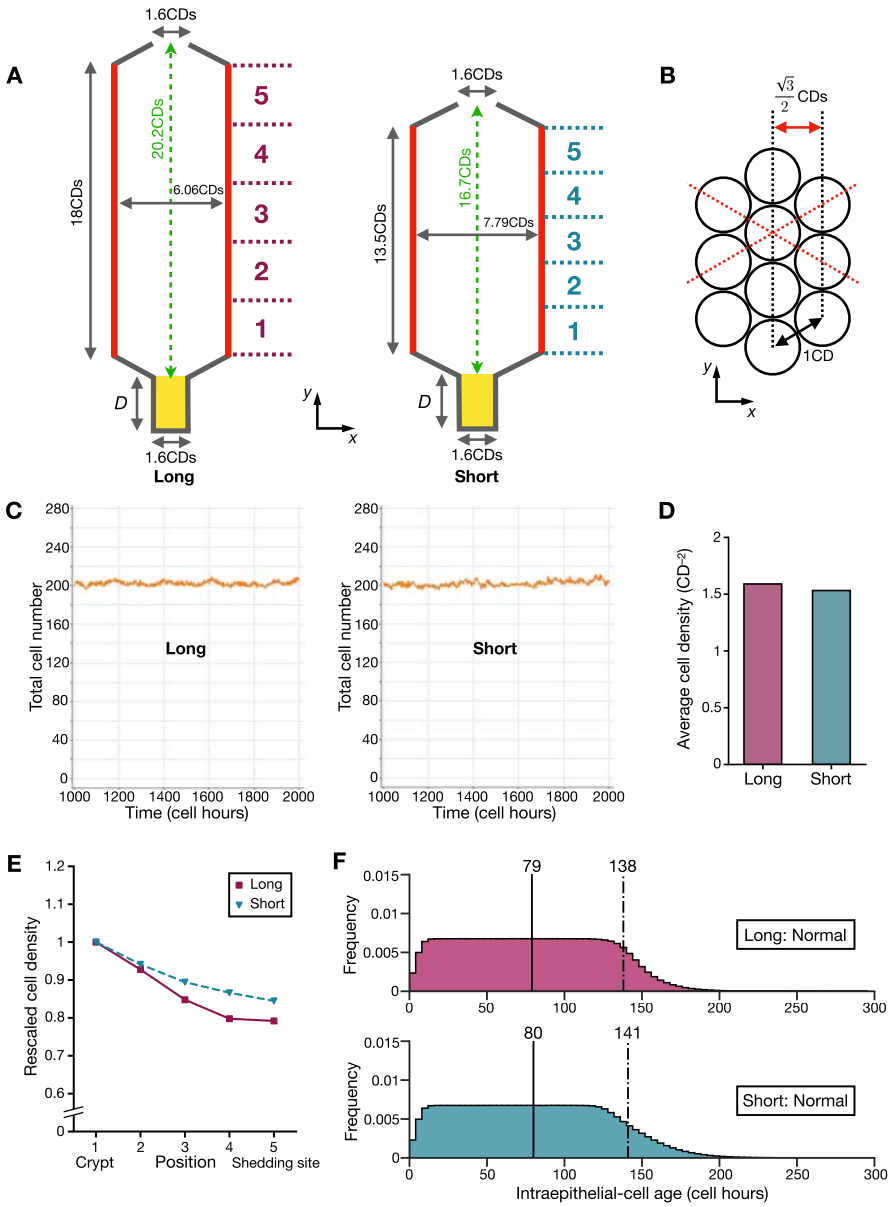

Figure S4: 2D plane cell-based model. (A) Given are the schematic outlines of the 2D models: Long (*left*) and Short (*right*). The crypt areas are colored yellow. D is the crypt depth, regulated to achieve equal cell proliferation rates among different conditions. Periodicity in the x-axis direction is applied at the red lines, and the reflective condition is applied to other black lines. The green arrows indicate the distances between the crypt orifices and the shedding sites. The purple and cyan numbers indicate zones for calculating local average cell density. (B) Shown is an arrangement of cells connected by springs of natural length. Each circle represents a cell. The red arrow represents the spacing between cell columns. Red dotted lines connect adjacent cell centers. (C–F) The results of the normal condition are shown. (C) Given are the total number of cells at steady state of the Long (*left*) and Short (*right*). (D) Shown is the average cell density. (E) Given are the rescaled average cell density profiles along the crypt–shedding site axis. Each position number corresponds to the same number of divided regions of Fig. S4A. (F) Shown are the intraepithelial-cell age distributions of the Long (*top*) and Short (*bottom*). The decreased frequency around age zero is because proliferative cells constitute the majority. The solid lines represent the average intraepithelial-cell ages, the dot–dash lines represent the old intraepithelial-cell age as indicated by the 90th percentile.

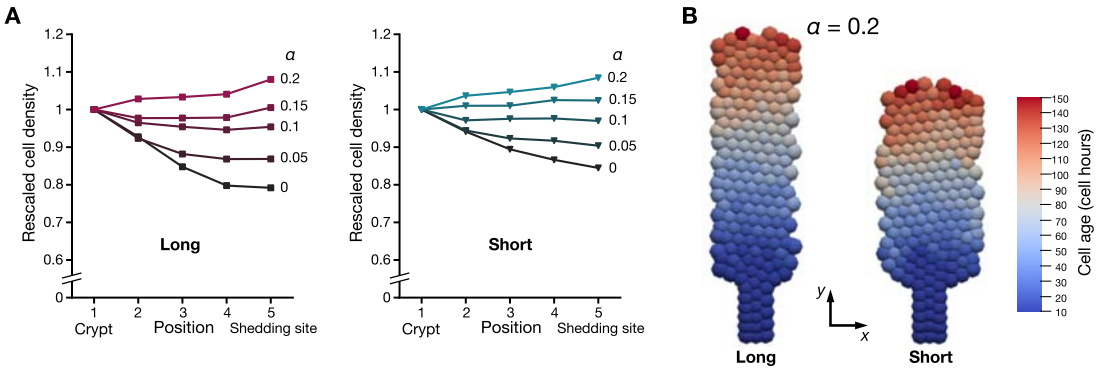

Figure S5: Effects of active cell migration. (A) Given are the rescaled average cell density profiles along the crypt–shedding site axis for various applied force magnitudes α of the Long (*left*) and Short (*right*). Each position number corresponds to the same number of divided regions of Fig. S4A. (B) Shown are cell age distributions in the surfaces at steady state for $\alpha = 0.2$ of the Long (*left*) and Short (*right*). Both shapes have the same color scale.

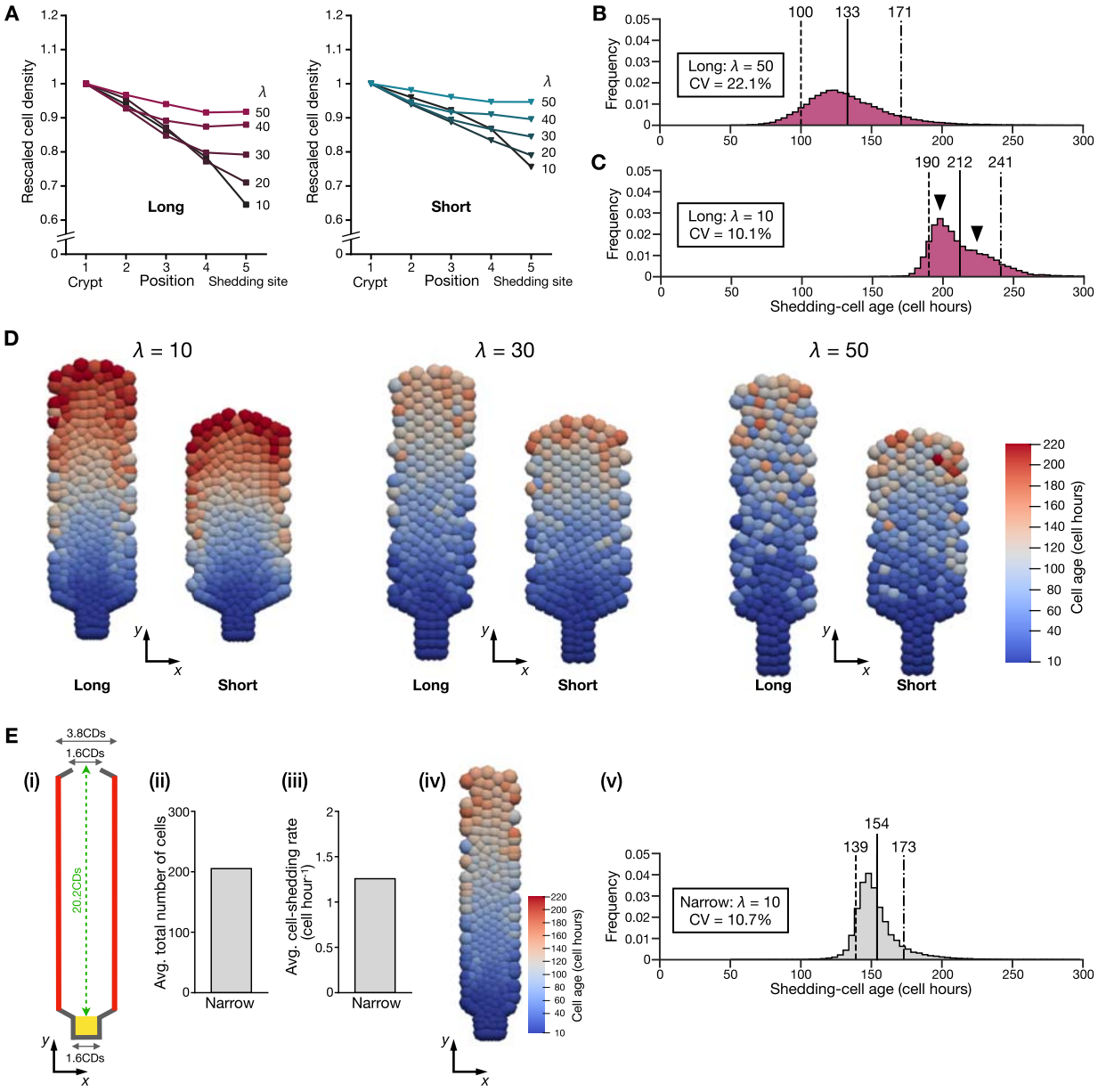

Figure S6: Effects of different material properties of cells. (A) Given are the rescaled average cell density profiles along the crypt–shedding site axis for various λ of the Long (*left*) and Short (*right*). Each position number corresponds to the same number of divided regions of Fig. S4A. (B, C) Shown are the shedding-cell age distributions of Long for $\lambda = 50$ (B), and $\lambda = 10$ (C). The dashed lines represent the early shedding-cell ages as indicated by 10th percentile of the shedding-cell ages, the solid lines represent the average shedding-cell ages, and the dot–dashed lines represent the late shedding-cell ages as indicated by the 90th percentile of the shedding-cell ages. Arrowheads indicate distribution bimodality. (D) Given are cell age distributions in the surfaces of the Long and Short at steady state for $\lambda = 10$ (*left panels*), $\lambda = 30$: the normal condition (*middle panels*), and $\lambda = 50$ (*right panels*). All conditions have the same color scale. (E) The results of the Narrow shape for $\lambda = 10$ are given. (i) Shown is the schematic of the Narrow shape; the crypt area is colored yellow, periodicity in the x-axis direction is applied at the red lines, and the reflective condition is applied to other black lines. The green arrow indicates the distance between the crypt orifice and the shedding site. (ii) Given is the average total number of cells in the model. (iii) Given is the average number of cells that shed per one cell hour. (iv) Given is the cell age distribution in the surface. (v) Given is the shedding-cell age distribution. The dashed line represents the early shedding-cell age, the solid line represents the average shedding-cell age, and the dot–dashed line represents the late shedding-cell age.

Supporting Movie Legends

Movie S1:
A movie showing the 3D surface cell-based model: Villus, Bump, and Disk.

Movie S2:
A movie showing the normal condition in the 2D plane cell-based model: Long and Short.

Movie S3:
A movie of active cell migration in the 2D plane cell-based model: Long and Short for $\alpha = 0.2$.

Movie S4:
A movie comparing different material properties of cells in the 2D plane cell-based model: Long and Short for $\lambda = 10$ (*left panels*), and Long and Short for $\lambda = 50$ (*right panels*).

Movie S5:
A movie showing the Narrow 2D plane cell-based model with $\lambda = 10$.

In all movies, proliferative cells are colored yellow and differentiated cells are colored white.

Table S1: Parameter Values in the 3D Surface Cell-Based Model

	μ	η
Villus	30	1.0
Bump	30	1.0
Disk	30	1.0

μ: connecting spring constant.
η: drag coefficient.

Table S2: Parameter Values in the 2D Plane Cell-Based Model

	Shape	μ	η	α	D (CD)
Normal condition	Long$^\sharp$	30	1.0	0	3.25
	Short$^\flat$	30	1.0	0	3.3
Active cell migration	Long$^\sharp$	30	1.0	0	3.25
	Short$^\flat$	30	1.0	0	3.3
	Long	30	1.0	0.05	3.45
	Short	30	1.0	0.05	3.45
	Long	30	1.0	0.1	3.63
	Short	30	1.0	0.1	3.6
	Long	30	1.0	0.15	4.0
	Short	30	1.0	0.15	3.9
	Long	30	1.0	0.2	4.25
	Short	30	1.0	0.2	4.15
Different material properties of cells	Long	10	1.0	0	1.95
	Short	10	1.0	0	2.15
	Long	20	1.0	0	2.8
	Short	20	1.0	0	2.9
	Long$^\sharp$	30	1.0	0	3.25
	Short$^\flat$	30	1.0	0	3.3
	Long	40	1.0	0	3.7
	Short	40	1.0	0	3.7
	Long	50	1.0	0	4.1
	Short	50	1.0	0	4.1
	Narrow	10	1.0	0	1.78

μ: connecting spring constant.
η: drag coefficient.
α: magnitude of the active cell migration force.
D: depth of the crypt.
$\sharp$: the same as Long of the normal condition.
$\flat$: the same as Short of the normal condition.

Supporting References

1. Krndija, D., F. El Marjou, B. Guirao, S. Richon, O. Leroy, Y. Bellaiche, E. Hannezo, and D. M. Vignjevic, 2019. Active cell migration is critical for steady-state epithelial turnover in the gut. *Science* 365:705–710.

2. Darwich, A. S., U. Aslam, D. M. Ashcroft, and A. Rostami-Hodjegan, 2014. Meta-analysis of the turnover of intestinal epithelia in preclinical animal species and humans. *Drug Metab. Dispos.* 42:2016–2022.

3. Mirams, G. R., C. J. Arthurs, M. O. Bernabeu, R. Bordas, J. Cooper, A. Corrias, Y. Davit, S. J. Dunn, A. G. Fletcher, D. G. Harvey, M. E. Marsh, J. M. Osborne, P. Pathmanathan, J. Pitt-Francis, J. Southern, N. Zemzemi, and D. J. Gavaghan, 2013. Chaste: an open source C++ library for computational physiology and biology. *PLoS Comput. Biol.* 9:e1002970.